PASSIVE NOSETIP TECHNOLOGY (PANT) PROGRAM

VOLUME XIX. HYDROMETEOR/SHOCK LAYER INTERACTION STUDY

ACUREX CORPORATION

PREPARED FOR

SPACE AND MISSILE SYSTEMS ORGANIZATION

AUGUST 1975

SAMSO-TR-74-86
Volume XIX

INTERIM REPORT
PASSIVE NOSETIP TECHNOLOGY
(PANT) PROGRAM

Volume XIX. Hydrometeor/Shock Layer Interaction Study

W. E. Nicolet
M. R. Wool
B. Laub
N. A. Jaffe

Aerotherm Division/Acurex Corporation

SAMSO-TR-74-86

August 1975

AEROTHERM REPORT 75-163

Air Force Space and Missile
Systems Organization
Los Angeles, California

Contract F04701-71-C-0027

C/N 7049.525

INTERIM REPORT
PASSIVE NOSETIP TECHNOLOGY
(PANT) PROGRAM

Volume XIX. Hydrometeor/Shock Layer Interaction Study

W. E. Nicolet
M. R. Wool
B. Laub
N. A. Jaffe

FOREWORD

This document is Volume XIX of the Interim Report series for the Passive Nosetip Technology (PANT) program. A summary of the documents in this series prepared to date is as follows:

Volume I — Program Overview (U)

Volume II — Environment and Material Response Procedures for Nosetip Design (U)

Volume III — Surface Roughness Data

Part I — Experimental Data

Part II — Roughness Augmented Heating Data Correlation and Analysis (U)

Part III — Boundary Layer Transition Data Correlation and Analysis (U)

Volume IV — Heat Transfer and Pressure Distributions on Ablated Shapes

Part I — Experimental Data

Part II — Data Correlation

Volume V — Definition of Shape Change Phenomenology from Low Temperature Ablator Experiments

Part I — Experimental Data, Series C (Preliminary Test Series)

Part II — Experimental Data, Series D (Final Test Series)

Part III — Shape Change Data Correlation and Analysis

Volume VI — Graphite Ablation Data Correlation and Analysis (U)

Volume VII — Computer User's Manual, Steady-State Analysis of Ablating Nosetips (SAANT) Program

Volume VIII — Computer User's Manual, Passive Graphite Ablating Nosetip (PAGAN) Program

Voluem IX — Unsteady Flow on Ablated Nosetip Shapes — PANT Series G Test and Analysis Report

Volume X — Summary of Experimental and Analytical Results

Volume XI — Analysis and Review of the ABRES Combustion Test Facility for High Pressure Hyperthermal Reentry Nosetip Systems Tests

Volume XII — Nosetip Transition and Shape Change Tests in the AFFDL 50 MW RENT Arc - Data Report

Volume XIII — An Experimental Study to Evaluate Heat Transfer Rates to Scalloped Surfaces — Data Report

Volume XIV — An Experimental Study to Evaluate the Irregular Nosetip Shape Regime — Data Report

Volume XV — Roughness Induced Transition Experiments — Data Report

Volume XVI — Investigation of Erosion Mechanics on Reentry Materials (U)

Volume XVII — Computer User's Manual, Erosion Shape (EROS) Computer Program

Volume XVIII — Nosetip Analyses Using the EROS Computer Program

Volume XIX — Hydrometeor/Shock Layer Interaction Study

Volume XX — Investigation of Flow Phenomena Over Reentry Vehicle Nosetips

Volume XXI — Flight Implications of Low Temperature Ablator Shape Data (U)

Volume XXII — Coupled Erosion/Ablation of Reentry Materials

Volume XXIII — Reentry Vehicle Nosetip Response Analyses (U)

This report was prepared by Aerotherm Division/Acurex Corporation under Contract F04701-71-C-0027. Volumes I through IX covered PANT activities from April 1971 through April 1973. Volumes X through XV represent contract efforts from May 1973 to December 1974. Volumes XVI through XVIII describe the background, development, and check out of the PANT EROsion Shape (EROS) computer code. These volumes document efforts performed under supplementary agreements to the Minuteman Natural Hazards Assessment program (Contract F04701-74-C-0069) between April 1974 and March 1975. Volumes XIX through XXIII document additional analyses performed between December 1974 and June 1975.

This work was administered under the direction of the Space and Missile Systems Organization with Lieutenant A. T. Hopkins and Lieutenant E. G. Taylor as Project Officers with Mr. W. Portenier and Dr. R. L. Baker of the Aerospace Corporation serving as principal technical monitors. Mr. W. E. Nicolet was principal Aerotherm investigator for the work described in this volume

This technical report has been reviewed and is approved.

E G Taylor

E. G. Taylor, Lt, USAF
Project Officer
Aero and Materials Division
Directorate of Systems Engineering
Deputy for Reentry Systems

TABLE OF CONTENTS

LIST OF ILLUSTRATIONS

LIST OF TABLES

LIST OF SYMBOLS

a	particle acceleration, or	ft/sec^2
	sonic velocity	ft/sec
a_n	see Equation (2-22)	--
atm	unit abbreviation, pressure	atmospheres
Bi	Biot modulus = hR_p/k_w	--
B'_o	dimensionless blowing rate (Equation (2-7))	--
Btu/lbm	unit abbreviation, enthalpy	British thermal unit/ pount-mass
C_H	Stanton number including blowing effect	--
C_{H_o}	nonblown Stanton number	--
f,f( )	functions of ( )	--
F	force accelerating particles	lbf
Fo	Fourier number	--
g,g( )	functions of ( )	--
h	heat transfer coefficient	Btu/ft^2sec-^oR
H_c	critical heat of formation per lbm	Btu/lbm
H_e	boundary layer edge recovery enthalpy	Btu/lbm
H_f	hydrometeor heat of formation per lbm	Btu/lbm
H_{tot}	total enthalpy	Btu/lbm
H_w	enthalpy of gases at hydrometeor surface	Btu/lbm
H_2	shock layer conditions at V_2	Btu/lbm
H_∞	free stream enthalpy	Btu/lbm

LIST OF SYMBOLS (Continued)

H_2O	chemical symbol for water atom	--
in.	unit abbreviation, distance	inches
k_{air}	thermal conductivity of air	Btu/ft-sec-°R
kft	unit abbreviation, distance	kilofeet
kft/sec	unit abbreviation, velocity	kilofeet/second
k_r	condensation rate coefficient	--
k_w	thermal conductivity of hydrometeor	Btu/ft-sec-°R
lbf	unit abbreviation, force	pounds-force
lbm	unit abbreviation, mass	pounds-mass
$\dot{m}$	mass flux	lb/ft^2sec
M	Mach number	--
M_p	particle mass	slugs
$\mathcal{M}$	molecular weight	lbm/lb-mole
Nu	Nusselt number = $2hR_p/k_{air}$	--
P	various pressures	atm
Pr	Prandtl number	--
q_o	stagnation point heating rate	Btu/ft^2sec
R_N	vehicle nose radius	in. or ft
R_p	hydrometeor radius	μm
t	time in shock layer	seconds
t_D	boundary layer mass diffusion time	sec
t_k	kinetic vaporization time	sec

LIST OF SYMBOLS (Continued)

t_{res}	total residence time in shock layer	seconds
T	instantaneous droplet surface temperature	°R
T_{vap}	vaporization temperature	°R
T_{∞}	free stream temperature	°R
u_e	boundary layer edge velocities	ft/sec
u,V	various velocities	ft/sec
$U_{1,2}$	edge velocities in Lock's problem	ft/sec
We	Weber number	--
y	surface normal direction	ft
x	streamwise distance in Lock's problem	ft
z	altitude	kft
α	thermal diffusivity	ft^2/hr
β	see Equation (2-24)	--
γ	specific heat ratio	--
δ	boundary layer thickness	ft
Δ	change in quantity	--
Δ_s	shock standoff distance	ft
$\epsilon\sigma T^4$	hydrometeor reradiation	Btu/ft^2sec
η	Lock's transformed coordinate	--
λ	blowing parameter	--
θ	angle around spherical droplet	degrees
μ	viscosity	lbm/ft-sec

μm	unit abbreviation	micrometers
ν	kinematic viscosity	ft^2/sec
π	pi, 3.1415926	--
ρ	density	lbm/ft^3
$\rho_e u_e$	boundary layer edge mass flux	lbm/ft^2sec
ψ	stream function	--

Subscripts

b	back of particle	--
bl	boundary layer	--
crit	critical condition for vaporization	--
D	diffustion from hydrometeor	--
e	boundary layer edge condition	--
K	kinetical controlled	--
p	hydrometeor properties	--
s	stagnation conditions on hydrometeor, or surface condition	--
SP	stagnation point	--
t	total conditions	--
w	surface conditions	--
z	behind normal shock	--
∞	free stream conditions, or infinity	--

Superscripts

'	conditions behind hydrometeor shock	--

SECTION 1

INTRODUCTION

Hypersonic vehicles during reentry may experience extensive damage due to encounters with condensed phase H_2O in the form of either ice particles or liquid droplets. These encounters can lead to augmented heating rates and mechanical erosion. The condensed phase H_2O particles, termed hydrometeors, must traverse the shocked gas enveloping the reentry vehicle prior to impacting the surface. The shock layer can, depending on flight conditions, vehicle configuration, and particle size, have a marked influence on the hydrometeors traversing the region between the shock wave and the body surface. Hence, an understanding of hydrometeor/shock layer interaction is required in order to predict impact conditions from specified vehicle configuration and free stream conditions.

This report documents the results of an investigation directed at surveying a portion of the phenomenology associated with the interaction between water droplets and strong shock waves. The investigation has concentrated on phenomena arising from heat transfer rather than from mechanical forces; treatments of stripping and wave formation (interface instability considerations) leading to catastrophic breakup touched upon are not treated in depth.

Under many conditions of interest, all or a portion of a liquid drop may attain supercritical pressures (and temperatures) giving rise to the question of what role, if any, is played by interfacial tension in inhibiting drop breakup. Accordingly, the possible liquid motion resulting from large pressure and density gradients is addressed and solutions are presented for the time required for significant droplet distortion under purely hydrodynamic forces.

This potential breakup mode does not consider surface tension, and to the authors' knowledge has not been considered previously. In Reference 1 tests at Mach numbers in the 1.5 to 3.5 range on 750 to 4500 μm size droplets, it was indicated that the primary mechanism for breakup is shear induced stripping. In Reference 2 it is hypothesized that at higher Mach numbers catastrophic breakup is dependent on Weber number.

For regimes of interest, the mass density of condensed phase materials is negligibly small compared to the mass density of gas in the free stream. Hence, the assumption can be made that the particulate matter will not significantly perturb the flow field.

Technology related to the present problem has been to a certain extent developed by investigators concerned with two phase flow in combustors and rocket nozzles. References 3 through 7 contain related work. Although the aforementioned references present results related to hydrometeor shock layer interactions, the governing parameters (i.e., particle properties, gas properties, and flow field conditions) differ from those of interest for this investigation. Waldman and Reinecke (Reference 2) treat the general problem of water droplet shock layer interactions for reentry flight conditions. The applicability of the results in Reference 2 is severely limited due to the adoption of numerous simplifying assumptions. In addition, the heat transfer from the gas to the particle is not treated correctly in Reference 2. References 8 and 9 contain corrections to the formulation of the heat transfer model given in Reference 2.

In References 2, 8 and 9 it was assumed that the droplet and surroundings were in chemical equilibrium and that conditions within the droplet and the gas were in steady state. Although relaxation times associated with potential particle/shock interaction phenomena are small, the particle residence time in the shock layer can be as small as fractions of a microsecond. Hence, it is necessary to validate the equilibrium/steady state assumptions. Once regimes for equilibrium, steady state flow have been defined, mass transfer coefficients can be employed to predict particle mass loss rates. Standard Nusselt number correlations as given in References 3 through 7 are only an approximation since mass transfer effects on Nusselt number were not included. In addition, results based on Nusselt number correlations with mass transfer corrections are still suspect since these correlations and corrections have not been experimentally validated for the specific conditions of interest in the present investigation. Hence, in order to obtain heat and mass transfer coefficients with a reasonable degree of reliability a limited number of calculations were performed in which these quantities were obtained from exact solutions to the multicomponent laminar boundary-layer equations.

Previous studies have indicated that shock layers will have negligible effects on particles in the rain drop size range (500 to 2500 μm); hence, attention has been focused on sub-100 μm diameter droplets. The pressure and enthalpy ranges considered correspond to altitude ranges from 20 to 40 kft, velocity ranges from 10 to 20 kft/sec, and nosetip radii of 0.75 and 2.5 inches.

In summary, a survey of particle shock interactions relative to the following phenomena have been made:

- Mechanical breakup
- Diffusion and kinetic limited mass loss
- Convective heat and mass transfer

It is emphasized that previous studies have considered the last item to be the significant thermal event. The present investigation does not treat the other phenomena in detail but focuses on determining the flight regimes and particle dimensions for which they will be significant.

The particle as it traverses the shock layer will, at least initially and in most cases until impact, be in a doubly shocked gas and hence an extremely severe hyperthermal environment. For convenience, a set of parameters that can be utilized to characterize certain pertinent particle and vehicle parameters has been generated and is presented in Appendix A. These include the following quantities as functions of vehicle altitude and Mach number:

- Free stream unit Reynolds number
- Sonic point unit Reynolds number
- Vehicle stagnation pressure
- Shock standoff (normalized with nose radius)
- Stagnation point momentum thickness (scaled with square root of nose radius)
- Vehicle total enthalpy
- Particle total enthalpy
- Particle Mach number
- Particle Weber number
- Particle stagnation pressure
- Particle unit Weber number

SECTION 2

ANALYSIS

The analysis is focused on characterizing thermally induced events taking place arising from free stream water droplets interacting with reentry vehicle shock layers. As was mentioned, mechanical breakup arising from high induced internal pressures is also considered. The particle size range considered in these analyses is smaller than that generally encountered in precipitating rain but is representative of that found in cloud formations. It is emphasized that the particle environment consists of a doubly shocked region and hence, in terms of enthalpy and pressure, it will be more severe than the vehicle shock layer. The range of conditions employed in the analyses is summarized below.

Configuration Condition

Nose radii: 0.75 and 2.50 in.

Free Stream Conditions

Altitude: 15-40 kft

Velocity: 10-20 kft/sec

Particle Conditions

R_p: 5-100 μm

P_s: 50-2000 atm

H_t: 5000 - 24,000 Btu/lbm

M_p: 2.4 - 2.9

Appendix A gives further details relating free stream conditions to particle and nosetip environmental conditions.

In Section 2.1, the entry of particles in a shock layer is described and a simple model is used to compute droplet distortions. Section 2.2 compares the times to achieve equilibrium mass diffusion with particle residence times and shows that convective film coefficient modeling in the shock layer is appropriate. Section 2.3 presents analyses of the convective

heat and mass transfer between a particle and the doubly-shocked, shock layer gases including particle transient thermal response calculations.

2.1 MECHANICAL BREAKUP

Mechanical forces are present in the shock layer of the vehicle (or induced in it) which tend to cause asymmetric loads on the water droplet and can cause it to break up. Initially, the droplet encounters asymmetric loads as it crosses the shock front. Subsequently, a quasi-steady gasdynamic flow is established about the droplet introducing shear forces along its surface (which are viewed as a stripping effect and not considered here) and a pressure difference between the stagnation point and other points on the surface of the droplet. The droplet cannot support such asymmetric loads and must respond hydrodynamically. If sufficient time is available before the droplet impacts the surface of the body, it can distort to the point where it can be viewed as having broken up. The sequence of events is shown in Figure 2-1, which were inferred from theoretical considerations.

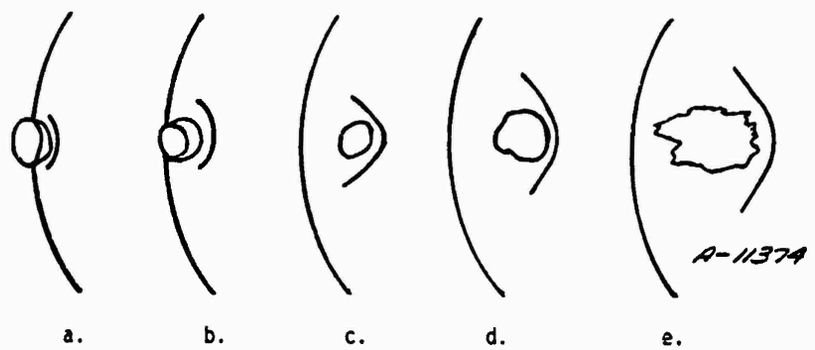

Figure 2-1. Droplet breakup phenomenology.

Entry Through the Shock Front

As the droplet enters the shock layer of the body, it displaces the shock front locally and simultaneously initiates a new gasdynamic shock wave inside the shock layer and a compression wave inside the droplet itself (Figures 2-1a and 2-1b). As the speed of sound in water is typically about 5000 ft/sec, or 1/3 to 1/2 the velocity of the droplet relative to the shock layer gases, the compression wave in the water will not have time to make a full traverse across the droplet before the latter is completely through the shock front and into the shock layer. It follows that there will be a region within the droplet where there is

undisturbed water. Thus, water droplets will always be able to pass through the shock front without breaking up, provided only that the droplet velocity is greater than the sound speed of water.

Traverse of the Shock Layer

A quasi-steady gasdynamic flow will be established about the droplet very quickly after the latter enters the vehicle shock layer. This supersonic flow will induce significant hydrodynamic pressure differences across the droplet. Of course, such pressure differences represent a potential driving force for flow within the droplet. Internal motion would cause distortions and possibly break up as indicated in Figures 2-1d and 2-1e. The magnitude of this effect can be estimated by the use of simple force laws.

Consider a droplet of spherical shape of initial radius R_p, density ρ, stagnation pressure P_s and a pressure P_b on its back side which can be neglected relative to P_s. The net force tending to accelerate the particle is then

$$F \sim P_s \pi R_p^2 \tag{2-1}$$

while the mass to be accelerated is

$$M_p \sim \frac{4}{3} \pi R_p^3 \rho_p \tag{2-2}$$

If the acceleration acts over a distance ΔR_p, which can also be viewed as the increase in radius of the particle due to distortion, then

$$\Delta R_p \sim \frac{1}{2} a t_{res}^2 \tag{2-3}$$

where a is the acceleration and t_{res} is the residence time of the droplet in the shock layer of the body. Then combining the above equations with

$$a = \frac{F}{M_p} \tag{2-4}$$

yields

$$\frac{\Delta R_p}{R_p} \sim \frac{P_s}{\rho_p R_p^2} t_{res} \tag{2-5}$$

which is the key result desired. The residence time, t_{res}, is fixed by the nose radius of the vehicle and, consequently, does not vary significantly. Likewise, the water density does not vary significantly, so that breakup is primarily a function of droplet radius and stagnation point pressure. Indeed, distortion (and hence, the likelihood of breakup) is seen to increase with the stagnation pressure and decrease with the size of the initial droplet radius, in rough agreement with the available experimental data. It is viewed as significant that surface tension does not play an important role in this model, in contrast to the model of Waldman and Reinecke (Reference 2)

A number of solutions to Equation (2-5) are presented in Table 2-1, considering interesting flight conditions and for a residence time of 2×10^{-7} seconds. As shown there, the 10 μm droplets are likely to break up for all the interesting pressures, as are the 20 μm droplets. The larger droplets will probably not break up, even at the highest pressures of interest.

TABLE 2-1. DROPLET DISTORTIONS

Pressure (atm)	500	1000	2000
Radius (μm)	$\Delta R_p/R_p$		
10	3.75	7.5	15.
20	0.94	1.88	3.76
50	0.149	0.298	0.596
100	0.0371	0.0752	0.1504

2.2 DIFFUSION AND KINETIC LIMITED MASS LOSS

If it is assumed that the hydrometeor surface is in vaporization equilibrium and radiation can be neglected, an established correlation exists between a parameter representing nondimensional blowing, B'_o, and an appropriate combination of total enthalpy, H_e, surface enthalpy, H_w, and heat of formation of surface material, H_f. The correlation is given by*

$$B'_o = \ln\left(1 + \frac{H_e}{H_w - H_f}\right) \qquad (2\text{-}6)$$

*This relation is identical to relations employed in Appendix C.

where

$$B_o' = \frac{\dot{m}_D}{\rho_e u_e C_{H_o}} \tag{2-7}$$

The quantity $\dot{m}_D$ is the diffusion limited surface mass flux normal to the surface and $\rho_e u_e$ is the mass flux parallel to the surface in the inviscid flow. In order to assess the significance of transient effects in limiting diffusion mass transfer, the time constant for this phenomenon must be compared to the particle residence time in the shock layer. The time constant appropriate for diffusion through the viscous layer is given by the ratio of mass in the boundary layer to diffusion mass

$$t_D = \left(\int_o^\delta \rho_{bl} dy\right) \Big/ \dot{m}_D \tag{2-8}$$

The integral for the boundary layer mass in the previous equation can be approximated by (Reference 10)

$$\int_o^\delta \rho_{bl} dy \approx 1.5\ Pr^{0.6} \left(\frac{\rho_e \mu_e}{\rho_e u_e C_{H_o}}\right) \tag{2-9}$$

and the value $\dot{m}_D$ is obtainable from Equations (2-6) and (2-7) for specified flight conditions.

Over the conditions of interest it can be shown that the quantity $(\rho_e u_e C_{H_o})$ is within the range 200 to 1000 lbm/ft^{2}sec. The quantity t_D is calculated for the high end of the droplet pressure range, which will be on the order of 2000 atm (see Appendix A). Table 2-2 contains time constants for the range of conditions of interest.

TABLE 2-2. DIFFUSION TIME CONSTANT t_D (SEC x 10^9) AT P = 2000 ATM

H_e (Btu/lbm)	$\rho_e u_e C_{H_o}$ (lbm/ft^{2}sec)		
	200	500	1000
5,000	40	7	1.7
10,000	20	3	0.8
15,000	8	1.3	0.3

Particle shock residence times for the stagnation region are of the order of 2×10^{-7} seconds, hence, from Table 2-2 it does not appear that transients are important in determining diffusion limited mass loss.

Once the steady boundary layer becomes filled with vaporization products, mass loss will be diffusion, rather than kinetic controlled. An estimate of the times associated with vaporization kinetic events can be made based on simple considerations. A rate equation of the form

$$\dot{m}_K = f(T_s) - k_r P_w \tag{2-10}$$

can be written to describe the heterogeneous vaporization process. The rate coefficient, k_r, can be evaluated from simple kinetic theory as follows:

$$k_r = 122 \times 10^6 \sqrt{\frac{m}{T_s(^\circ R)}} \quad \text{lbm/ft}^2\text{sec-atm} \tag{2-11}$$

This expression includes a sticking factor of units which has an uncertainty of perhaps a factor of 25. Using the steam table (Reference 11) and detailed balancing, the net forward rates can be estimated as follows:

Temperature, T_s (°R)	Vapor Pressure (atm)	$\dot{m}_K$ (lb/ft^{2}sec)
575.	0.1	2×10^6
672.	1.0	2×10^7
817.	10.0	2×10^8

Pressures of actual interest are much higher than given above, but the trend to higher $\dot{m}_K$ values with increasing pressure is clear. Above the critical pressures, vaporization kinetics modeling is not clear but since the process is homogeneous, faster rates should occur.

The time required to supply the boundary layer with vaporization products is a measure of the time when vaporization kinetics would be signfiicant. This time, t_K, may be estimated from

$$t_K = \left(\int_0^\delta \rho_{bl} dy\right)/\dot{m}_K \tag{2-12}$$

Typical values for heat transfer coefficient values of interest are given in Table 2-3.

TABLE 2-3. KINETIC TIME CONSTANT t_K (SEC x 10^{13}), P = 2000 ATM

T_s (°R)	$\rho_e u_e C_{H_o}$ (lbm/ft²sec)		
	200	500	1000
575	50	20	10
672	5	2	1
812	0.5	0.2	0.1

Again since hydrometeor residence times are on the order 2×10^{-7} seconds, it is safe to assume that vaporization kinetics are not significant.

The above analyses mean that continuum, equilibrium, fluid mechanics apply in the vicinity of a hydrometeor and that boundary layer modeling can be used to investigate hydrometeor/shock layer interactions. Film coefficient modeling of heat and mass transfer events is described is the following section.

2.3 CONVECTIVE HEAT AND MASS TRANSFER

The air flowing about the surface of a water droplet (immersed in a shock layer) is subjected to shock heating by two successive near-normal shock fronts. The levels of pressure and enthalpy which result give the air the potential for delivering exceedingly high convective heating rates to the droplet surface. If such heating rates are, in fact, delivered, one would expect significant mass removal from the droplet by ablation. The prediction of the coupled convective heating-ablative response is made complicated and uncertain by a number of factors not usually encountered in conventional problems.

The novel features of this problem stem from the fact that the water can behave much like a gas at the supercritical pressures of interest. Therefore, a free shear layer will exist along the air-water boundary in which both the air and water co-exist and are responding mechanically. Questions immediately arise with regard to the proper treatment of the physical events. It is important to employ a solution procedure which couples the motion of the water to that of the air? Alternately, can the droplet surface be approximated as being stationary? What are the parameters which govern the problem? Further, as there is no phase change between the water in the droplet and the water which has diffused into the surrounding air, how does one decide if mass has been removed from the droplet or not? Also, one would expect to have

a significant amount of mass removed by stripping if existing theories are to be believed (Reference 2). Will mass transfer effects significantly reduce the stripping effect? Indeed, is the mass stripped from the front half of the droplet removed from the droplet or merely moved to its backward-facing half? Finally, when is it appropriate to consider steady-state fluid-dynamic and ablative response events, and when must transient events be considered?

In the material presented in the following paragraphs a number of the questions raised with regard to proper modeling approaches are discussed. The objective of this material is to reduce this exceedingly complex problem to a point where valid estimates of the ablative mass losses can be obtained.

Inviscid Flow Parameters

The inviscid, adiabatic flow field events of interest include the pressure distribution and boundary layer edge velocity and enthalpy. The results of an "exact" solution were used to obtain the pressure distributions assuming an invariant spherical shape.* The boundary layer edge velocities were obtained by calculating an isentropic expansion to the local pressure. Finally, the stagnation point pressures and enthalpies were obtained using a procedure (the ACE program, Reference 12) which solves the Rankine-Hugoniot equations governing the double shock system, coupled to the equations governing the equilibrium chemical state. The free stream, downstream (after the initial shock), and stagnation point solutions for the flight conditions of interest are presented in Tables 2-4, 2-5, and 2-6, respectively. Additional material on the inviscid flow will be presented and discussed with the discussion of the convective heating events.

Air/Water Mixing Region

The air/water mixing region ultimately determines the amount of mass removed from the front surface of the droplet; consequently, a solution to its governing equations** would represent a major step toward the solution of the ablation problem. To the authors' knowledge solutions of this type are not available in the literature. Moreover, the generation of such

---

*Of course, this represents an approximation as the droplet shape will change (in general) as it traverses the shock layer. Shape change effects could have been considered but it was felt that they would greatly complicate the analysis without adding appreciably to the understanding of the essential physical events.

**The mixing region is governed by the boundary layer equations (global mass, momentum, energy and diffusion) which must be solved subject to both a valid set of transport properties and to a chemical equilibrium constraint valid from both the pure gas phase (air) into the pure liquid phase (water).

TABLE 2-4. FREESTREAM PROPERTIES

z (kft)	M_∞	V_∞ (ft/sec)	P_∞ (atm)	T_∞ (°R)	ρ_∞ (lb/ft^3)	H_∞ (Btu/lb)	a_∞ (ft/sec)
15	10	10574.	0.56450	465.22	0.04814	-17.152	1057.4
	15	15861.					
	20	21148.					
20	10	10369.	0.45989	447.42	0.04077	-21.424	1036.9
	15	15554.					
	20	20738.					
25	10	10161.	0.37165	429.62	0.03431	-25.696	1016.1
	15	15242.					
	20	20322.					
30	10	9948.	0.29756	411.84	0.02866	-29.963	994.8
	15	14922.					
	20	19896.					
35	10	9731.	0.23596	394.06	0.02375	-34.230	973.1
	15	14597.					
	20	19462.					
40	10	9681.	0.18576	389.97	0.01890	-35.212	968.1
	15	14522.					
	20	19362.					

Note: $H_\infty = 0.24\ (T_\infty - T_{ref})$ (Btu/lb) where $T_{ref} = 536.698°R$ (298.16°K)

TABLE 2-5. DOWNSTREAM PROPERTIES

z (kft)	M_∞	M_2	V_2 (ft/sec)	P_2 (atm)	T_2 (°R)	ρ_2 (lbs/ft^3)	m_2	H_2 (Btu/lb)	H_{tot} (Btu/lb)
15	10	0.34091	1306.	69.849	6953.47	0.38990	28.35	2182.3	2215
	15	0.30828	1657.	159.837	11772.25	0.46089	24.79	4953.4	5008.
	20	0.29027	1918.	288.062	16003.76	0.53074	21.53	8843.4	8916.
20	10	0.34273	1292.	56.814	6755.46	0.32731	28.42	2093.0	2126.
	15	0.30777	1625.	130.169	11379.34	0.39012	24.91	4758.5	4811.
	20	0.29112	1889.	234.494	15586.88	0.44757	21.73	8498.3	8570.
25	10	0.34463	1278.	45.851	6557.29	0.27285	28.50	2004.1	2036.
	15	0.30716	1593.	105.195	10978.15	0.32837	25.03	4564.4	4615.
	20	0.29023	1860.	189.410	15168.39	0.37487	21.92	8155.0	8221.
30	10	0.34662	1264.	36.657	6357.01	0.22559	28.57	1915.0	1947.
	15	0.30660	1558.	84.230	10567.25	0.27454	25.15	4369.5	4418.
	20	0.29301	1831.	151.574	14744.58	0.31147	22.13	7810.5	7878.
35	10	0.34868	1250.	29.020	6155.10	0.18490	28.64	1826.1	1857.
	15	0.30622	1522.	66.803	10153.71	0.22781	25.29	4175.9	4222.
	20	0.29404	1801.	120.114	14315.99	0.25660	22.33	7467.3	7532.
40	10	0.34892	1244.	22.857	6089.80	0.14714	28.63	1806.1	1837.
	15	0.30543	1507.	52.646	9989.08	0.18218	25.25	4132.2	4178.
	20	0.29341	1783.	94.656	14088.97	0.20527	22.31	7390.1	7454.

TABLE 2-6. PARTICLE SHOCK LAYER PROPERTIES

z (kft)	M_∞	M'_∞	M'_2	V'_2 (ft/sec)	P'_2 (atm)	T'_2 (°R)	ρ'_2 (lbs/ft^3)	H'_2 (Btu/lb)	H'_{tot} (Btu/lb)
15	10	2.4193	0.47592	2317.	438.739	10263.70	1.5599	3791.0	3898.2
	15	2.6426	0.44274	3005.	1236.497	17336.81	2.1787	8803.3	8983.6
	20	2.9103	0.41341	3644.	2624.119	23197.38	2.8009	15965.	16230.
20	10	2.4079	0.47640	2270.	353.789	9907.50	1.3086	3635.9	3738.9
	15	2.6381	0.44404	2959.	1005.571	16851.23	1.8364	8459.3	8634.2
	20	2.9049	0.41294	3557.	2129.008	22464.86	2.3717	15343.	15595.
25	10	2.3954	0.47718	2225.	282.838	9556.29	1.0894	3481.5	3580.4
	15	2.6318	0.43874	2894.	850.622	16556.53	1.5844	8292.3	8459.6
	20	2.8808	0.41260	3471.	1712.971	21744.65	1.9936	14723.	14964.
30	10	2.3814	0.47833	2180.	223.769	9209.64	0.89861	3326.5	3421.4
	15	2.6299	0.44707	2868.	649.758	15871.90	1.2793	7772.8	7937.1
	20	2.8909	0.41241	3387.	1364.423	21031.21	1.6613	14101.	14330.
35	10	2.3657	0.47985	2136.	175.125	8867.98	0.73398	3171.7	3262.9
	15	2.6306	0.44872	2822.	515.290	15376.54	1.0555	7431.8	7590.9
	20	2.8834	0.41237	3303.	1075.624	20327.52	1.3718	13480.	13698.
40	10	2.3664	0.47897	2117.	138.083	8736.13	0.58652	3138.6	3228.1
	15	2.6378	0.44770	2794.	408.529	15132.04	0.84852	7360.0	7515.9
	20	2.8928	0.41067	3260.	853.453	19940.12	1.1070	13351.	13563.

where $M'_\infty = \dfrac{V_\infty - V_2}{a_2}$

solutions is beyond the scope of the present study. Fortunately, problems have been studied (and solutions published) which include many of the essential features of the present problem. Solutions to such problems give qualitative features and are useful in guiding the construction of approximate solution procedures.

R. C. Lock (Reference 13) considered the two-dimensional motion of a stream of fluid with velocity, U_1, density, ρ_1, and viscosity, μ_1, over a parallel stream with velocity, U_2, density, ρ_2, and viscosity, μ_2. Both fluids were assumed to be incompressible. The configuration is shown in Figure 2-2.

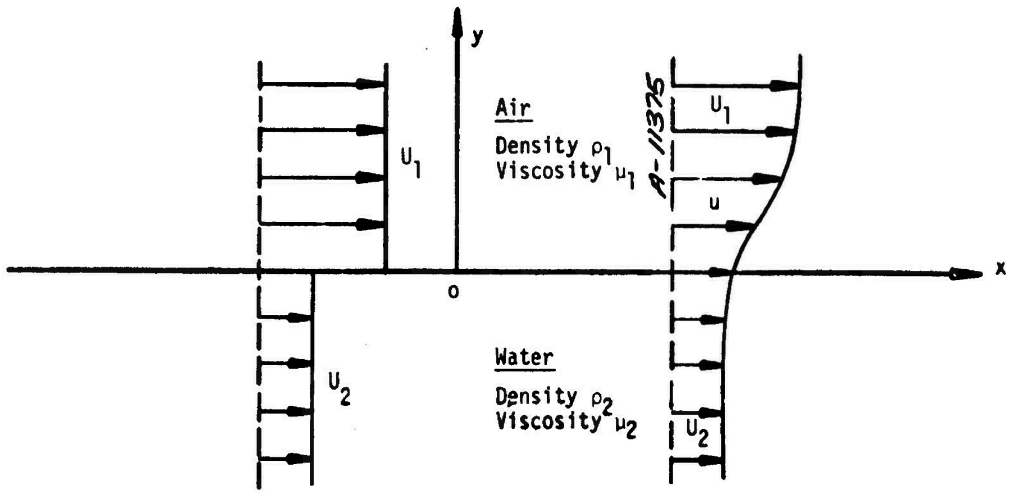

Figure 2-2. Mixing layer configurations.

The equations and boundary conditions are written out in Appendix B. Self-similar solutions were obtained in terms of the coordinate

$$\eta_1 = \left(\frac{U_1}{\nu_1 x}\right)^{1/2} y \tag{2-13}$$

for the upper stream and the coordinate

$$\eta_2 = \left(\frac{U_1}{\nu_2 x}\right)^{1/2} y \tag{2-14}$$

for the lower stream.

Numerical solutions to Lock's problem are presented in Figure 2-3 for the interesting case of $U_2 = 0$ and for a range of viscous density ratios ($\equiv \rho_2\mu_2/\rho_1\mu_1$). It is significant that the magnitude of the viscous density ratio alone determines the importance of the coupling

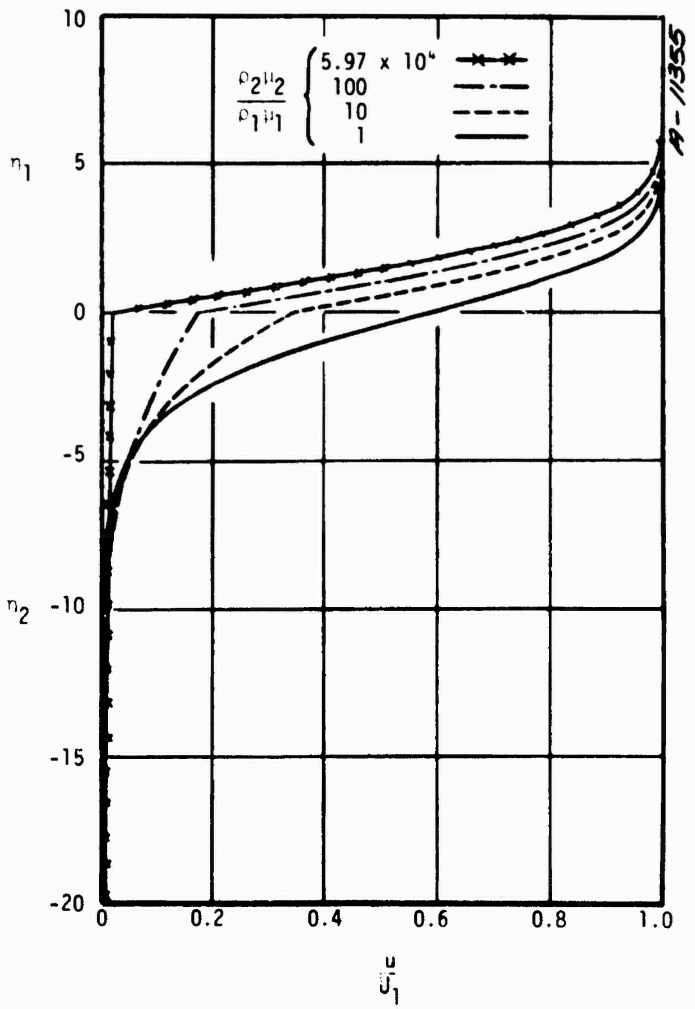

Figure 2-3. Solutions to Lock's problem.

between the two streams. Thus, for values of this parameter greater than or equal to roughly 100, one should be able to approximate the upper stream as a boundary layer over a stationary wall. Indeed, if mass transfer effects were included, this number would probably be somewhat lower. This result should also be applicable to the air/water mixing region over the droplet; that is, if

$$\rho_{water}\mu_{water}/\rho_{air}\mu_{air} \sim O(100)$$

the motion of the water can be uncoupled from the motion of the air.

Typical values of density and viscosity are presented in Table 2-7 for air edge conditions and for water. As shown, the viscous density ratio is often ~O(100), thereby justifying uncoupling the water flow from the air flow. Based on this conclusion, unblown convective heating rates were computed from boundary layer theory for conditions and droplet sizes of interest. These are discussed below.

TABLE 2-7. DENSITIES AND VISCOSITIES

Air			
P (atm)	ρ_1 (lb/ft^3)	μ_1 (lb/ft-sec)	$\rho_1\mu_1$
943	1.197	1.244×10^{-4}	1.5×10^{-4}
1900	2.155	1.313×10^{-4}	2.83×10^{-4}
2910	3.027	1.366×10^{-4}	4.1×10^{-4}
Water			
T (°K)	ρ_2 (lb/ft^3)	μ_2 (lb/ft-sec)	$\rho_2\mu_2$
50	62.4	3.66×10^{-4}	$228. \times 10^{-4}$
100	62.4	1.9×10^{-4}	$117. \times 10^{-4}$

Unblown Convective Heating Rates

The analysis was limited to spherical droplets traversing the shock layer on the vehicle stagnation streamline. Solutions were obtained to the laminar, nonsimilar, chemically reacting boundary layer equations using a detailed, numerical procedure (the BLIMP code, Reference 14). Vehicle free stream conditions encompassed one altitude range from 15-40 kft and vehicle Mach numbers from 10 to 20. The vehicle free stream conditions were taken from Reference 15 and are summarized in Table 2-4. Conditions behind the vehicle shock were obtained from normal shock ACE solutions (Reference 12), and are summarized in Table 2-5. The free stream conditions

behind the particle shock were also obtained from normal shock ACE solutions using conditions behind the vehicle shock as the properties upstream of the particle shock. These results, which are used as the free stream conditions for the BLIMP calculations, are summarized in Table 2-6. Note that, for the flight conditions considered, particle Mach numbers (M'_∞) lie in the narrow range from 2.4 to 2.9.

Pressure distribution around the sphere was obtained from an "exact" solution to the inviscid flow field around a sphere. The ratio of local static pressure to stagnation pressure (P/P_s) is shown in Figure 2-4 for an upstream Mach number of 1.8. The flow field over the rear hemisphere is not well-characterized since separation occurs in the region $90° < \theta < 120°$. Therefore, heating predictions were only made over the windward side of the sphere, i.e., $0° \leq \theta \leq 90°$.

Heat transfer distributions were calculated for droplet sizes from 5 to 100 μm at 15 kft and 40 kft for free stream Mach numbers of 10, 15, and 20. Predicted distributions of cold-wall heat transfer coefficient are shown in Figure 2-5 for altitudes of 40 kft and 15 kft, respectively. These results were correlated and the similarity of the distributions suggested a curve fit. The heat transfer distribution can be represented in terms of the stagnation point values as:

$$\frac{\rho_e u_e C_{H_o}}{(\rho_e u_e C_{H_o})_{SP}} = \begin{cases} \cos\theta & \text{for} \quad 0° \leq \theta \leq 60° \\ \frac{1}{2}\exp[-(\theta-60)/(90-60)] & \text{for} \quad 60° \leq \theta \leq 90° \end{cases} \tag{2-15}$$

The stagnation point heat transfer was correlated and can be represented by:

$$[\rho_e u_e C_{H_o}]_{SP} = 33\sqrt{P_\infty/R_p}\, M_\infty^{1.32} \tag{2-16}$$

where $[\rho_e u_e C_{H_o}]_{SP}$ = stagnation point heat transfer coefficient, lbm/ft^{2}sec

P_∞ = free stream static pressure, atm

R_p = droplet radius, μm

The applicability of the correlation was shown by comparing the nondimensional distribution to BLIMP results for a droplet with a radius of 50 μm at 25 kft for Mach numbers of 15 and 20. The results of this comparison is shown in Figure 2-6. Estimates of the heat transfer in the separated region range from 1 to 4 percent of stagnation. The average heat transfer over the front half of the sphere is 71 percent of stagnation.

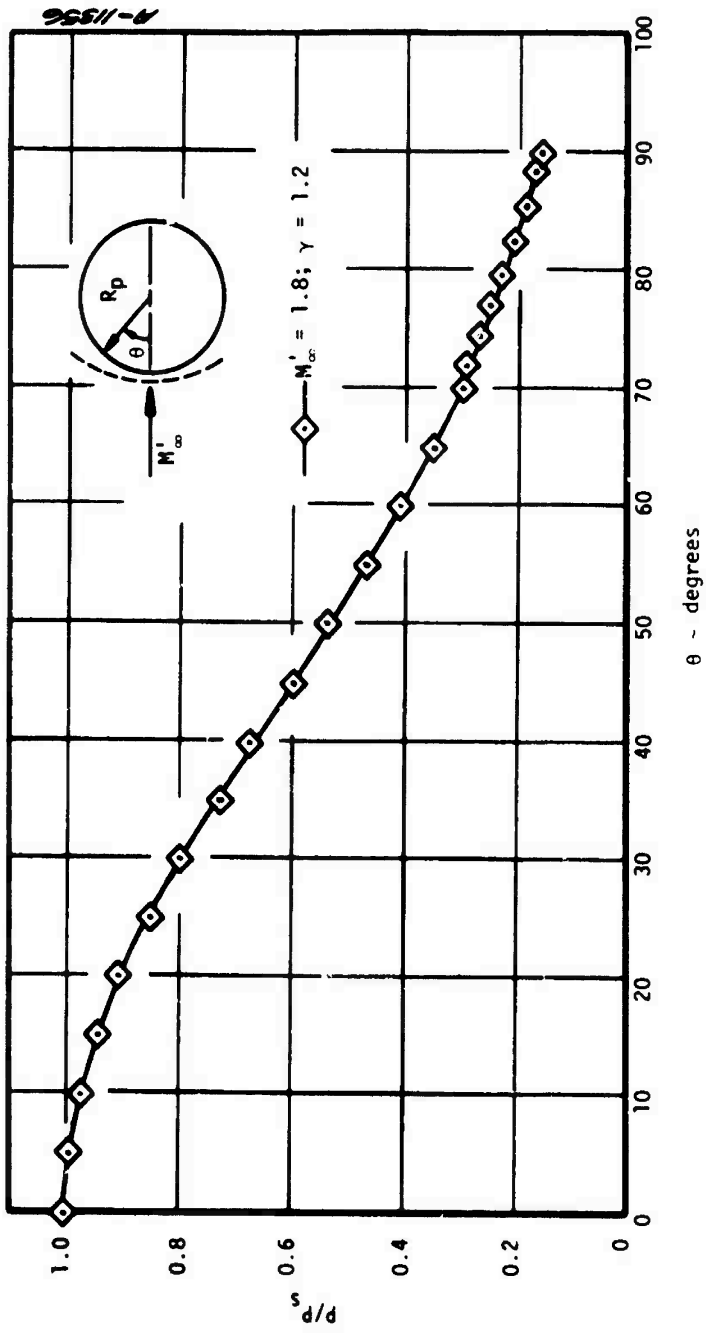

Figure 2-4. Sphere pressure distribution.

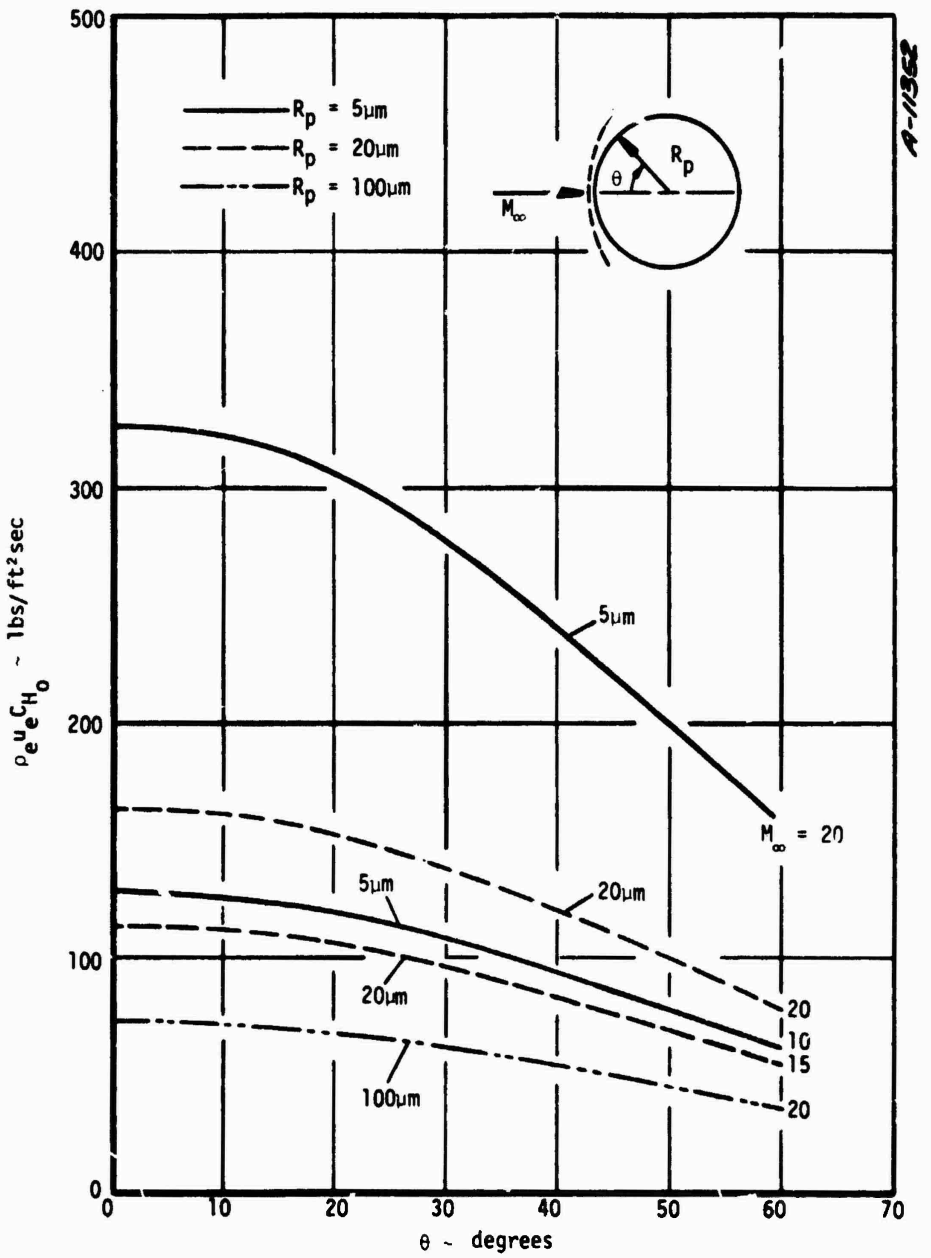

Figure 2-5. Heat transfer coefficient distributions in doubly shocked air (computed using BLIMP code, Reference 16).

a. Altitude = 40 kft

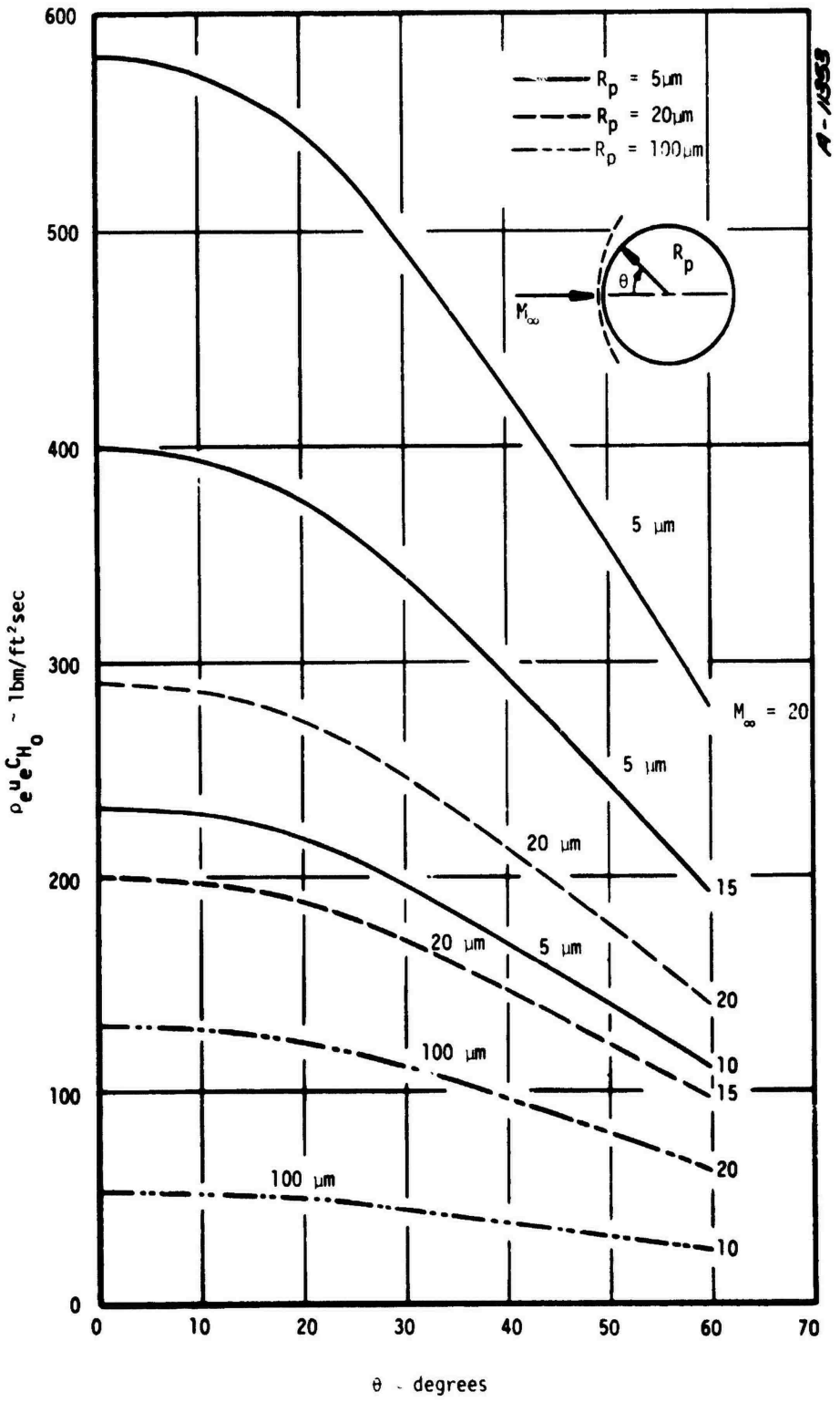

Figure 2-5. Concluded

b. Altitude = 15 kft

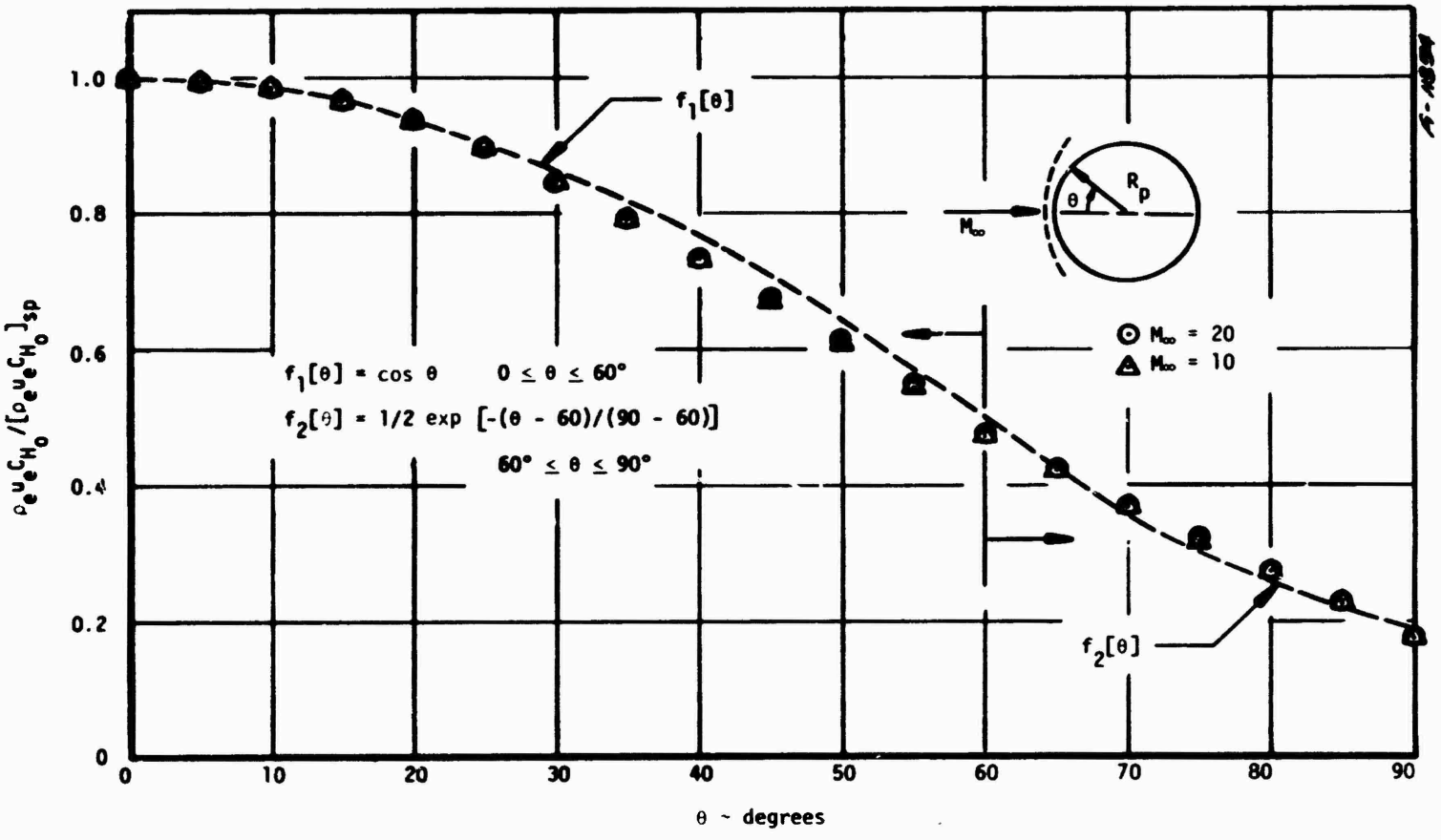

Figure 2-6. Comparison of heat transfer distribution correlation result to BLIMP result for altitude = 25 kft, particle radius = 50 μm.

Values of the cold wall heating rates are also useful and are tabulated along with transfer coefficient and total enthalpy values in Table 2-8 for the droplet stagnation point conditions. Note that the rates are in the range 2×10^5 to 10×10^6 Btu/ft^{2}sec which are huge relative to those encountered by reentry vehicles in even the most severe reentry environments.

Transient Heat Conduction

Despite the significant heating rates experienced by the particle, vaporization will not take place if the surface temperature is below its saturation value. It is pointed out that conditions including pressure, and hence saturation temperatures, vary around the droplet during its traverse of the shock layer. Moreover, prediction of this variation, especially past separation, is exceedingly difficult and matters are complicated by the existence of a supercritical state for certain flow conditions. Since the present calculations are designed to determine for which flight regimes various mechanisms need be considered, approximations are made. Thus, the time to attain the saturation temperature for $P \approx P_s$, used as a measure of the surface relaxation time for vaporization. It is also assumed that the hydrometeors are spherical.

The unsteady heat conduction solution for the surface of a heated sphere initially at T_∞ exposed to a temperature T_2' is given by

$$\frac{T_s(t) - T_\infty}{T_2' - T_\infty} = f(Fo,Bi) \tag{2-17}$$

where

$$Fo = \alpha_w t/R_p^2 \tag{2-18}$$

$$Bi = \frac{hR_p}{k_w} \tag{2-19}$$

The heat transfer coefficient, h, can be obtained from the stagnation point convective heating correlation given as Equation (2-16). That is,

$$h = C_{p,air}\, \rho_e u_e C_{H_o} = 33 \sqrt{P_\infty/R_p}\, M_\infty^{1.32}\, C_{p,air} \tag{2-20}$$

TABLE 2-8. STAGNATION POINT COLD WALL HEATING RATES (q_o)

z (kft)	M_∞	R_p (μm)	q_o (Btu/ft²sec)	$[\rho_e u_e C_{H_o}]_{SP}$ (lb/ft²sec)	H'_{tot} (Btu/lbm)
40	20	5	4,431,000	327	13,563
↓	↓	20	2.216,000	163	↓
↓	↓	100	990,900	73	↓
↓	15	20	↓	113	7,516
↓	10	5	↓	129	3,228
25	20	50	2,207,000	147	14,964
↓	15	↓	880,600	104	8,459
15	20	5	9,412,000	580	16,230
↓	↓	20	4,706,000	290	↓
↓	↓	50	2,977,000	183	↓
↓	↓	100	2,105,000	130	↓
↓	15	5	3,583,000	399	8,983
↓	↓	20	1,791,000	199	↓
↓	10	5	903,400	232	3,898
↓	↓	100	202,000	51	↓

Heat transfer coefficient values given by the above analysis indicate Nusselt numbers which are 2 to 4 times the values given by typical low Mach number correlations such as those used in Reference 2, 8, and 9. If the Fourier number (Fo) is very small, the solution represented by Equation (2-14) assumes the semi-infinite plate form. That is, for

$$Fo \ll 1$$

$$\frac{T_s(t) - T_\infty}{T_2' - T_\infty} = g(Bi\ \sqrt{Fo}) \tag{2-21}$$

It is pointed out that residence times in the shock layer will be of the order of a microsecond; the thermal diffusivity α of water can be taken as 1.8×10^{-6} ft^2/sec; hence, for droplets on the order of 10 μm, the value of Fo is of the order 10^{-3}. For flight conditions of interest the Biot numbers (Bi) fall generally within the following range:

$$1 \leq Bi \leq 100$$

Values of Fourier number will be not greater than 10^{-2}. The functions f(Bi,Fo) and g(Bi,$\sqrt{Fo}$) satisfying Equations (2-17) and (2-21) are

$$f = 1 - 2\sum_{n=1}^{\infty}\left[\frac{\sin a_n - a_n \cos a_n}{a_n^2 - a_n \cos a_n \sin a_n}\right](\sin a_n)e^{-a_n^2} \tag{2-22}$$

where a_n are roots of $a_n \cot a_n = (Bi - 1)$

$$g = 1 - [1 - erf(Bi,\sqrt{Fo})]_e^{Bi^2 Fo} \tag{2-23}$$

Comparisons of values for the exact solution given by Equation (2-22) to the semi-infinite slab solution given by Equation (2-23) are shown in Table 2-9.

TABLE 2-9. VALUES OF $(T_s - T_\infty)/(T_2' - T_\infty)$

Bi	Fo	Exact Solution	Semi-Infinite Plate Solution	% Error
1	0.010	0.1128	0.1035	8.24
1	0.001	0.0357	0.0347	2.70
100	0.010	0.9528	0.9414	1.19
100	0.001	0.8362	0.8292	0.83

These results indicate the adequacy of the simpler approximate solutions; thus Equation (2-23) is employed to yield the surface temperature time relationship for droplets in the shock layer. For most conditions of interest this equation will be accurate to within less than 1 percent.

It is pointed out that the heat transfer coefficient correlation, given previously, requires no mass transfer correction since the present calculation is to establish times required to reach vaporization temperatures; thus, this portion of the analysis is related to heat transfer effects prior to substantial vaporization.

Surface temperature T_s is computed using $T_s = T_\infty$ at $t = 0$ as an initial condition. Values are to be compared to time intervals corresponding to the particle residence time, t_{res}, in the shock layer, which is given by

$$t_{res} = \frac{1}{\beta V_\infty} [\exp(\beta \Delta_s) - 1] \qquad (2\text{-}24)$$

where

$$\beta = \frac{3}{8} C_D \frac{\rho_s}{\rho_p} \frac{1}{R_p}$$

In the analysis, a hypersonic approximation for the shock standoff distance is employed, so that

$$\Delta_s / R_N = 0.08$$

Also

$$C_D = 1.0$$

Based on these assumptions, the approximate residence times of the hydrometeor in the shock layer along the vehicle stagnation line are as follows

	Residence Times – μsec		
	$M_\infty = 10$	$M_\infty = 15$	$M_\infty = 20$
$R_N = 0.75$ in.	0.6	0.4	0.3
$R_N = 2.50$ in.	1.9	1.3	1.0

Variations in altitude and drop size over the range of interest changes the above values less than ±20 percent.

The time required for a particle to achieve a condition where vaporization commences must be less than the residence time for convective mass loss to be significant. Since the droplets are typically at supercritical pressures for flight conditions of interest, the vaporization condition is not well defined. For the purpose of this simple analysis, vaporization is assumed to commence when droplet surface temperature reaches the critical point temperature, T_s = 1165°R. For a particular altitude and Mach number condition the left-hand side of Equation (2-21) can be evaluated. Then, Equations (2-18), (2-19), and (2-20) can be used to evaluate the time, t, to achieve vaporization.

Figure 2-7 presents the times to achieve vaporization conditions as a function of the droplet radius for a wide range of altitude and Mach number conditions. Figure 2-8 shows the time to achieve vaporization as a function of local heat transfer coefficient. Transfer coefficient partially correlates the results. A further collapse is obtained by correlating with the stagnation point heat flux. That is

$$q_o = \rho_e u_e C_{H_o} |_{SP} \cdot H'_{tot} \propto \sqrt{P_\infty / R_p}\, M_\infty^{1.32} \cdot M_\infty^2 \qquad (2\text{-}25)$$

Based on this approximation, time to reach critical temperature at the droplet stagnation point is given by

$$t_{crit} = 1050 \left(\sqrt{P_\infty / R_p}\, M_\infty^{3.3}\right)^{-2} = \frac{1050\, R_p}{P_\infty\, M_\infty^{6.6}} \ \mu\text{sec} \qquad (2\text{-}26)$$

where P_∞ = free stream pressure, atm

R_p = initial droplet radius, μm

M_∞ = free stream Mach number

t_{crit} = has units of μsec

Clearly the critical time is quite sensitive to the vehicle Mach number. As Figures 2-7 and 2-8 show, critical times to reach vaporization conditions at the droplet stagnation point are well below droplet residence times for typical reentry flight conditions

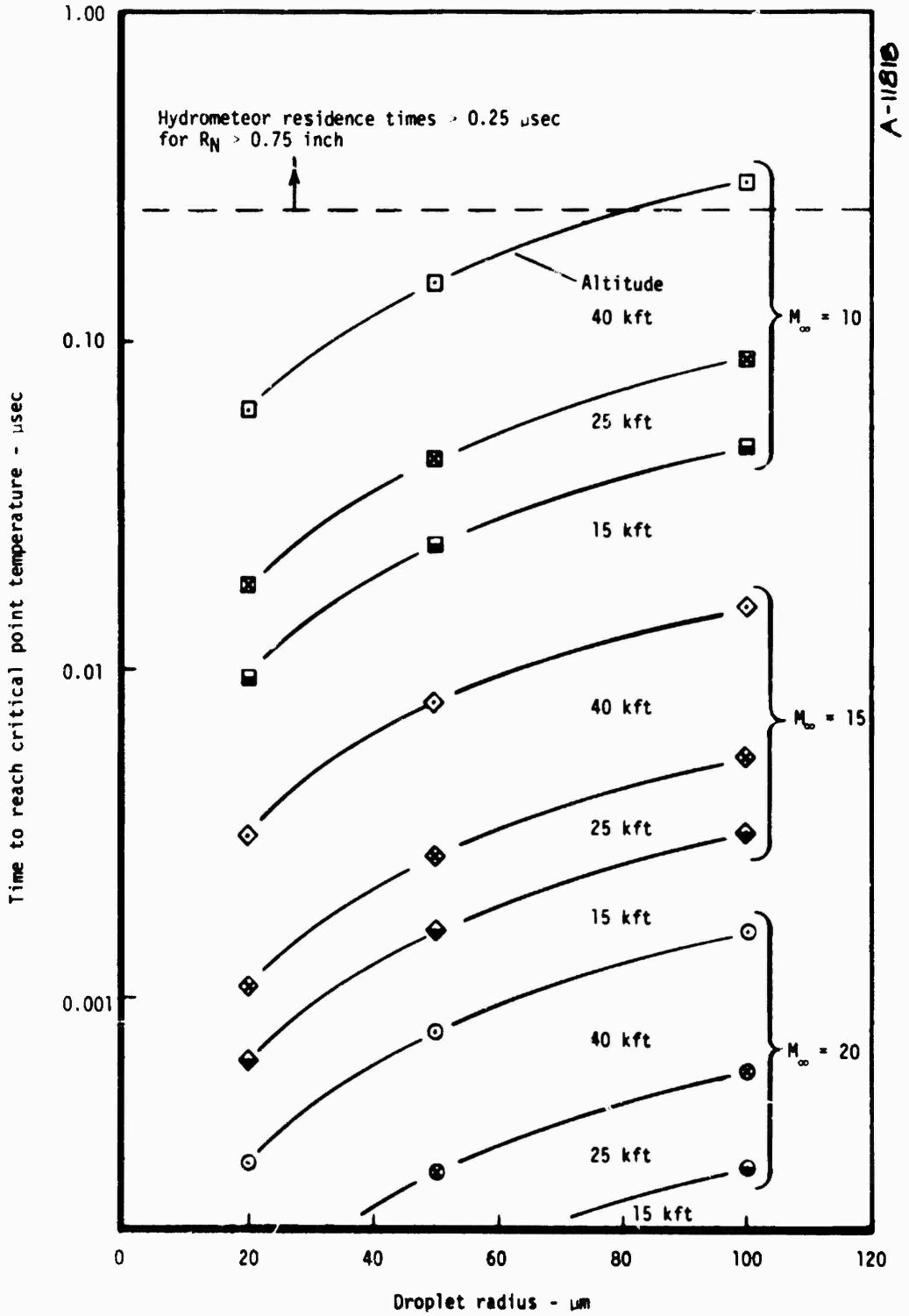

Figure 2-7. Droplet vaporization initiation.

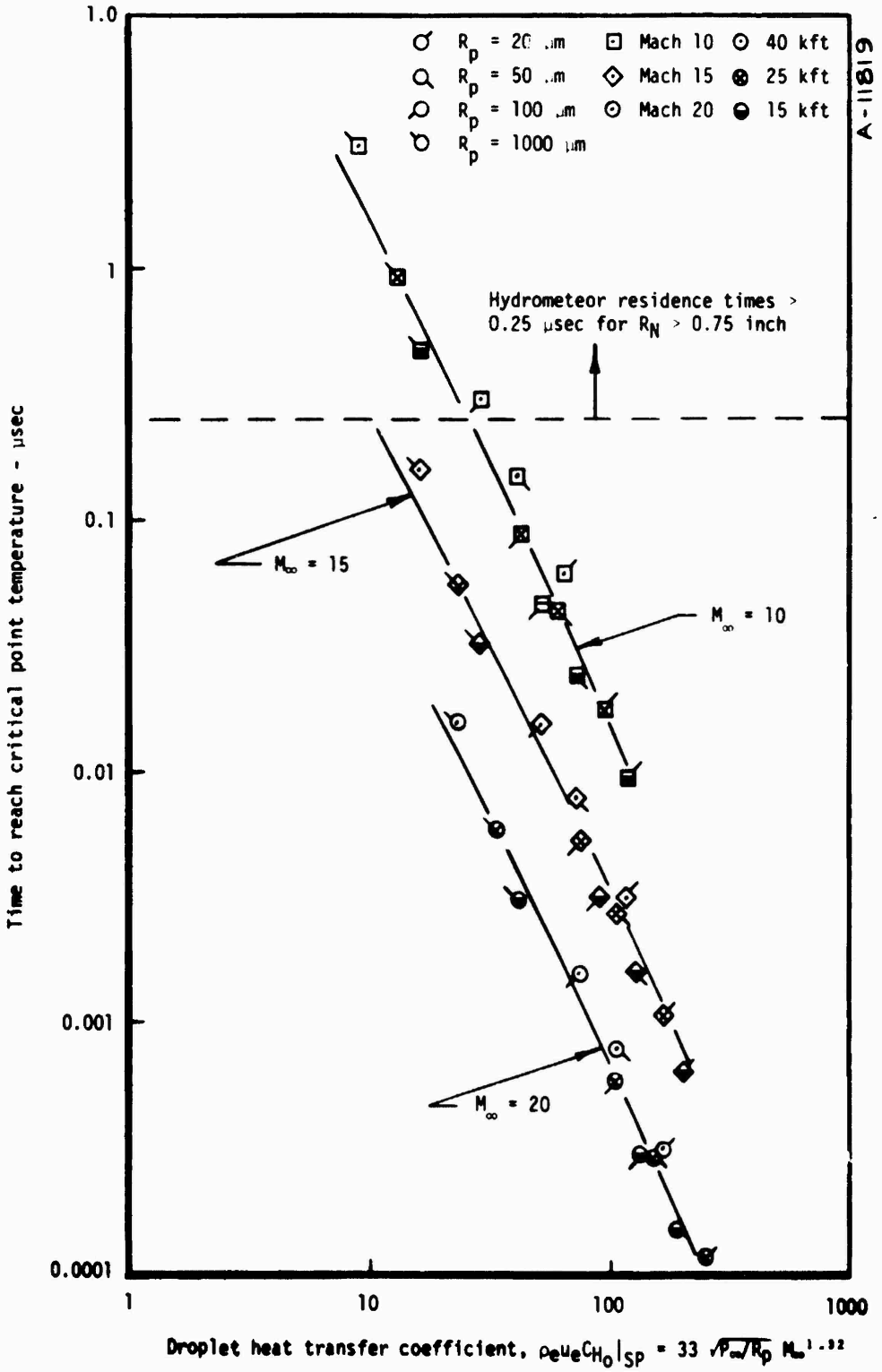

Figure 2-8. Partial correlation of droplet vaporization initiation.

It should be pointed out that previous experimental work by AVCO (Reference 16) and Aerotherm (Reference 17) was for snock velocities not exceeding 11.7 kft/sec. This work indicates that the principle shock/droplet interaction phenomena consists of droplet acceleration, stripping, and breakup. Inability to detect vaporization in these experiments of 100+ μm particles can, according to the present analysis, be partially attributed to the fact that surface temperatures did not reach vaporization levels. Consequently, although the aforementioned experiments do not indicate that vaporization is taking place it cannot be concluded that the effect of this phenomenon is unimportant for all flight conditions.

Mass Transfer Effects on Convective Heating

In the event that conditions are such as to produce vaporization, the effects of blowing on convective heating should be considered in the evaluation of mass loss. The neat blockage effects have traditionally correlated through a blowing correction to the Stanton number of the form (Reference 18).

$$\frac{C_H}{C_{H_o}} = \frac{2\lambda B'_o}{\exp(2\lambda B'_o) - 1} \quad . \qquad (2\text{-}27)$$

where

$$B'_o = \frac{\dot{m}_D}{\rho_e u_e C_{H_o}} \qquad (2\text{-}28)$$

and where λ is a parameter with a value that is a function of whether the flow is laminar or turbulent and is a function of the molecular weight of the ablated vapors. The results of a study by Bartlett, Nicolet and Howe (Reference 19) are presented in Figure 2-9, where it is shown that the correlation is excellent, the effect of molecular weight is second order, and a value $\lambda = 0.6$ does well in correlating the laminar data. At significantly higher blowing rates which are characteristic of water droplet vaporization, a higher order of λ would be applicable. However, since a higher value would minimize droplet mass loss, the 0.6 value is used in subsequent numerical work to estimate the upper limit of droplet mass loss.

Droplet Mass Loss by Ablation

The coupled drag and ablation of a droplet was computed for the conditions of interest. The approach of Jaffe (References 8 and 9) was modified to include the effects of blowing and real gas properties on the heat and mass transfer about the droplet. Appendix C presents the derivation and discussion of the hydrometeor mass loss and velocity equations which account

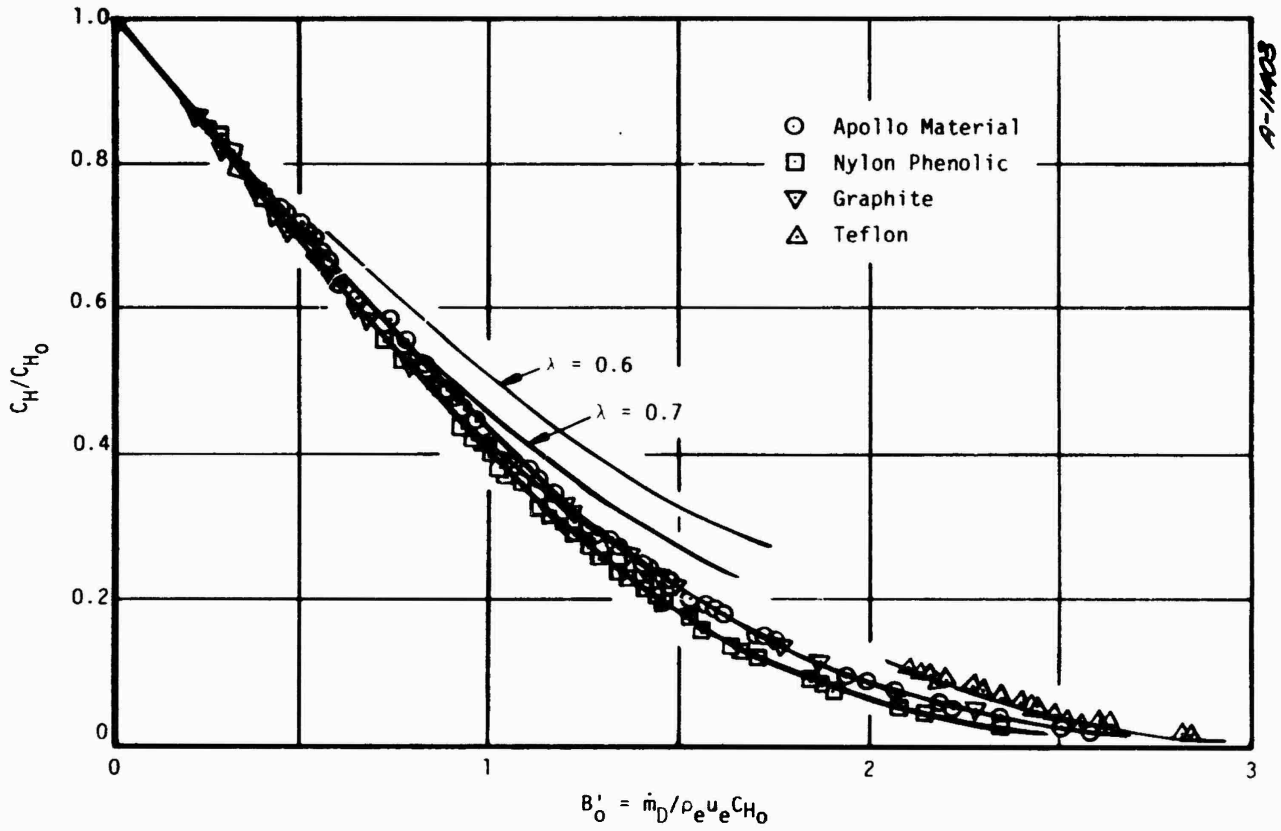

Figure 2-9. Reduction of Stanton number due to surface mass addition (from Reference 11).

for the above effects. The relations for droplet velocity and mass after the droplet passes through the shock layer are as follows:

$$\left.\begin{aligned} U_f &= U_\infty \exp\left[-\frac{2K_D}{K'_E}\left(1 - \sqrt{1 - 3/2\ K'_E}\right)\right] \\ M_{p,f} &= M_{p,i}\left(1 - 3/2\ K'_E\right)^2 \end{aligned}\right\} \quad 0 < K'_E < 2/3 \qquad (2\text{-}29)$$

where

$$K_D = \frac{3}{8} C_D \left(\frac{\rho_2}{\rho_p}\right) \frac{\Delta_s}{R_{p,i}}$$

$$K'_E = \frac{0.71\ \Delta_s\ [\rho_e u_e C_{H_o}]_{SP}|_i\ \ln\left[1 + 2\lambda\ H'_{tot}/Q^*_p\right]}{4\lambda\ (U_\infty - U_2)\ \rho_p\ R_{p,i}}$$

In the above relations subscript i denotes conditions existing on the particle at initial entry in the shock layer. For example, $[\rho_e u_e C_{H_o}]_{SP,i}$ indicates the initial particle stagnation-point heat transfer coefficient as it enters the shock but prior to any acceleration or ablation occurs. The transfer coefficient can be obtained from Equation (2-16) for $R_p = R_{p,i}$.

Note that $K'_E = 2/3$ corresponds to complete ablation before the droplet reaches the nosetip, and $K'_E = 2/3$ determines the critical conditions for no hydrometeor impacts.

Assumptions contained within Equations (2-29) are as follows:

- Stagnation point heat transfer scales with $u/\sqrt{R_p}$ as derived by Bartlett and Putz (Reference 20)
- Heat transfer to the back of the droplet is negligible
- Average heat flux to the front of the droplet is 71 percent of the stagnation point flux
- Rate of energy storage in the droplet is negligible compared to convective and vaporization energy rates.

Other details of the formulation are given in Appendix C.

Figure 2-10 shows hydrometeor mass reduction results for Mach 20 conditions as a function of shock standoff distance. For nose radii and drop dimensions of interest in this study, final mass is always more than 85 percent of initial mass even for very small hydrometeors.

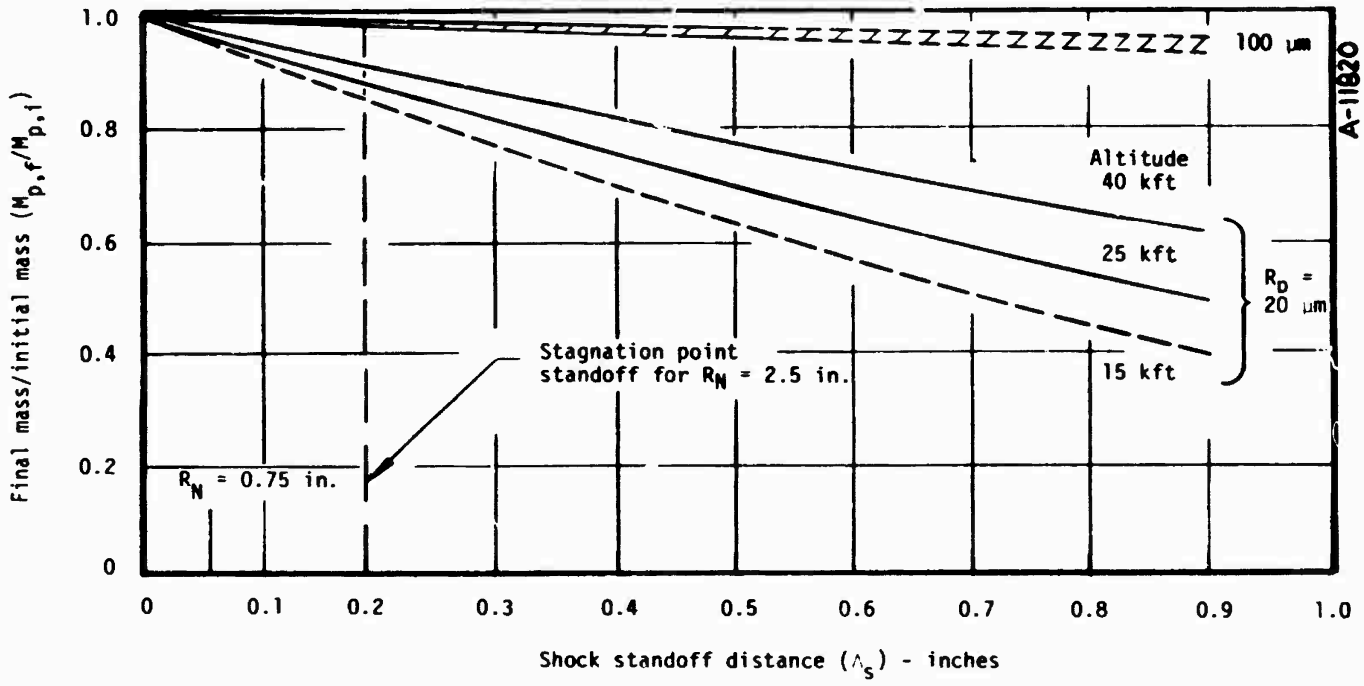

Figure 2-10. Hydrometeor mass loss results for free stream Mach number = 20.

For larger shock standoff distance, such as might apply to off-stagnation point locations, mass loss of the particle becomes more significant.

Hydrometeor slowdown results for the Mach 20 conditions are shown in Figure 2-11. The figure indicates that, although mass loss is small, particle velocity may be changed significantly, particularly for smaller particles.

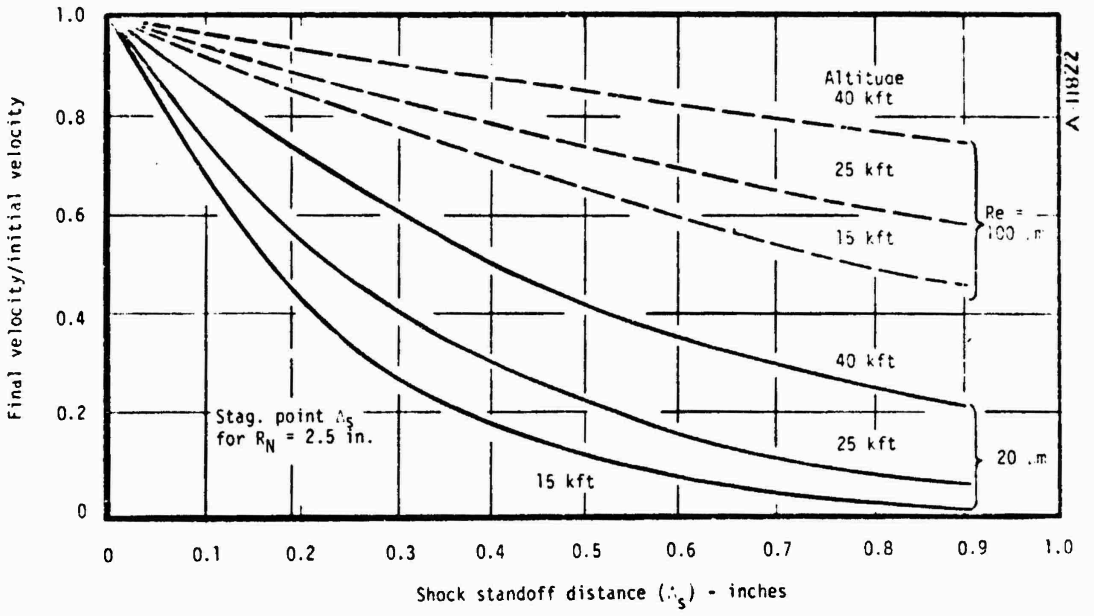

Figure 2-11. Hydrometeor slowdown results for free stream Mach number = 20.

SECTION 3

CONCLUSIONS AND RECOMMENDATION

On the basis of the present study, the following conclusions were reached relative to the prediction of mass losses from droplets immersed in reentry vehicle shock layers:

- Smaller particles, $R_p < 20$ μm, break up and need not be considered in a thermal response analysis.
- The viscous density ratio determines the characteristics of the mixing region about the droplet; current analysis indicates that the air motion can be decoupled from the water motion.
- For flight regimes and particle sizes of interest, the semi-infinite slab assumption is adequate for predicting transient surface temperatures.
- Transient response of hydrometeors need not be considered in droplet mass loss calculations unless the freestream Mach number is below 10.
- Heating events for the unblown air boundary layer about the droplet were obtained and correlated.
- Ablative mass loss of a hydrometeor was found to be less than 15 percent of the initial mass of the droplet for all particle sizes and Mach number conditions of interest.

In summary, these analyses have indicated that rain particle with radii greater than 20 μm remain essentially intact as they traverse the bow shock layer in the stagnation region of a high speed reentry vehicle. Particles smaller than 20 μm radius are likely to break up from the aerodynamic pressure in the shock layer, but particles larger than 20 μm will survive either because transient thermal response keeps the drop below vaporization temperatures (low Mach number), or because the hydrometeors do not lose significant mass. Particles in the 20 to 100 μm radius range do experience some slowdown (relative to the vehicle).

Based on these analyses, it is, therefore, recommended that coupled hydrometeor slowdown and ablation calculations including blowing effects be performed at conditions where

droplet vaporization is anticipated. Experimental verification of droplet transient response is recommended for particle diameters in the 100 to 300 μm range at Mach number greater than 10. Such testing would also indicate the effects of the super-critical surface state and droplet shape distortion effects on the conclusions reached here.

REFERENCES

1. Ranger, A. A. and Nicholls, J. A., "Aerodynamic Shattering of Liquid Drops," AIAA J., Vol. 7, No. 2, pp. 285-290, February 1969.

2. Waldman, G. D. and Reinecke, W. G., "Particle Trajectories, Heating and Breakup in Hypersonic Shock Layers," AIAA J., Vol 9, No. 6, pp. 1040-1043, 1971.

3. Hogland, R. F., "Recent Advances in Gas-Particle Nozzle Flows," ARS J, 32, 662-671, 1962.

4. Gilbert, M., Allport, J., and Dunlap, R., "Dynamics of Two-Phase Flow in Rocket Nozzles," ARS J., 32, pp. 1929-1930, 1962.

5. Carlson, D. J. and Hogland, R. F., "Particle Drag and Heat Transfer in Rocket Nozzles," AIAA J., Vol 2, No. 11, pp. 1980-1984, 1963.

6. Penner, S. S. and Williams, F. A., "Progress in Astronautics and Aeronautics, Vol. 6, Detonation and Two-Phase Flow," Academic Press, New York, 1962.

7. Wolfhard, H. G., Glassman, I., and Green, L., Jr., "Progress in Astronautics and Aeronautics, Vol. 14, Heterogeneous Combustion, Academic Press, 1964.

8. Jaffe, N. A., "Particle Decelration and Heating in a Hypersonic Shock Layer," Aerotherm TN-73-18, February 1973.

9. Jaffe, N. A., "Droplet Dynamics in a Hypersonic Shock Layer," AIAA J., Vol. 11, No. 11, pp. 1562-1564, November 1973.

10. Kreith, F., Principles of Heat Transfer, International Textbook Company, Scranton, N.J., 1963.

11. Keenan and Keys, Thermodynamic Properties of Steam, J. Wiles and Sons, Inc., New York, N.Y., 1965.

12. Powars, C. A. and Kendall, R. M., "User's Manual Aerotherm Chemical Equilibrium (ACE) Computer Program," unnumbered report, Aerotherm Corporation, Mountain View, California, May 1969.

13. Lock, R. C., "The Velocity Distribution in the Laminar Boundary Layer Between Parallel Streams," Quarterly Journal of Mech. and Applied Math., Vol. IV, Pt. 1, pp. 42-63, 1951.

14. Anderson, L. W. and Morse, H. L., "User's Manual Boundary Layer Integral Matrix Procedure (BLIMP)," Report No. AFWL-TR-69-114, Vol. 1 (Supp.), Air Force Weapons Laboratory, October 1971.

15. U. S. Standard Atmosphere Supplements, 1966. Prepared under sponsorship of Environmental Science Services Administration, National Aeronautics and Space Administration, United States Air Force.

16. Reinecke, W. G. and Waldman, G. D., "Shock Layer Shattering of Cloud Drops in Reentry Flight," AIAA Paper 75-152, presented at 13th Aerospace Sciences Meeting, Pasadena, California, January 20-22, 1975.

17. Jaffe, N. A., "Experimental Investigation of the Interaction Between Strong Shock Waves and Water Droplets," Aerotherm Report 75-156, Contract DNA001-74-C-0051, Aerotherm Division, Acurex Corporation, July 1975.

18. Dorrance, W. H., Viscous Hypersonic Flow, McGraw-Hill Book Co., 1962.

19. Bartlett, E. P., Nicolet, W. E., and Howe, J. T., "Heat Shield Ablation at Superorbital Re-Entry Velocities," Journal of Spacecraft and Rockets, 1971, p. 456.

20. Bartlett, E. P. and Putz, K. E., "Heat Transfer and Ablation-Rate Correlations for Re-Entry Heat Shield and Nosetip Applications," Journal of Spacecraft and Rockets, 1973, p. 15.

APPENDIX A

ENVIRONMENTAL TRAJECTORY CHARTS

by

M. D. Jackson

Reentry parameters for a vehicle and a particle entering the vehicle shock layer are presented in this Appendix. The parameters are defined as a function of velocity and altitude. The range of velocities and altitudes considered was 30 to 0 kft/sec and 60 to 1 kft.

The ACE code (Reference A-1) was used to characterize the environmental parameters. Calculations were performed for air, with ionization and dissociation considered. Table A-1 lists the species which were used in the calculations. Diffusion factors (F_{ij}) were also used in the computations, and are defined at the end of Table A-1. Freestream environmental properties of the atmosphere, namely density, pressure, temperature and sonic velocity are summarized in Figures A-1, A-2, A-3, and A-4 respectively.

Table A-2 summarizes the parameters calculated, their associated symbol, units, definition and correpondir[illegible]ure number. The following parameters listed in Table A-2 are related to the environment of a particle entering the vehicle shock layer:

- particle stagnation pressure and total enthalpy
- unit Weber number
- unit Reynolds number
- particle Mach number

In the ACE code it is assumed that gas mixture can be treated as a collection of thermally perfect species. Real behavior of gas mixtures become important as the mixture approaches its critical state. However, for the pressures and temperatures presented herein, these effects are insignificant.

REFERENCES FOR APPENDIX A

A-1. Powars, C. A. and Kendall, R. M., "User's Manual, Aerotherm Chemical Equilibrium (ACE) Computer Program," unnumbered report, Aerotherm Corporation, Mountain View, California, May 1969.

TABLE A-1. SPECIES THERMOCHEMICAL DATA

```
          AEROTHERM CHEMICAL EQUILIBRIUM JOB                    4120300000

RELATIVE ELEMENTAL COMPOSITIONS, ATOMIC WTS/UNIT MASS
    AT,NO.   ELEMENT     ATOMIC WT     COMPONENT 1  COMPONENT 2  COMPONENT 3
       7     NITROGEN    14.00800      .0532410     .0000000     .0000000
       8     OXYGEN      16.00000      .0143000     .0000000     .0000000
      18     ARGON       39.94800      .0006350     .0000000     .0000000
      99     ELECTRON      .00050      .0000000     .0000000     .0000000
 1. 99 0.  0 0.  0 0.  0 0.  0 0.  0 0.  OJANAF TAPE 7/71  3/65          E-
   -.81100+00   .13423+05   .49680+01   .50407-08   .11896+01   .10459+02 2500,0000 1
   -.81100+00   .13423+05   .49679+..   .92195-08   .23745+03   .10459+0220000,0000 1*******
 1. 7 0.  0 0.  0 0.  0 0.  0 0.  0 0.  OGILMORE - JANAF                N
    .11290+06   .13220+05   .37100+01   .38452-03   .10094+07   .40059+02 6000,0000 1
    .11290+06   .15916+05   .60975+01   .79158-04  -.47303+08   .40798+0220000,0000 1  .0316
 1. 8 0.  0 0.  0 0.  0 0.  0 0.  0 0.  OGILMORE -JANAF                 O
    .59559+05   .13494+05   .45713+01   .64557-04   .23355+05   .50115+02 6000,0000 1
    .59559+05   .12320+05   .38736+01   .14580+03   .10477+08   .49795+0220000,0000 1  .0009
 2. 8 0.  0 0.  0 0.  0 0.  0 0.  0 0.  OGILMORE - JANAF                O2
    .21500+00   .23277+05   .46197+01   .33147-03  -.79144+06   .67982+02 6000,0000 1
    .21500+00   .19995+05   .12604+02  -.34960-01   .28929+07   .67111+0220000,0000 1 1,1444
 1. 7 1.  8 0.  0 0.  0 0.  0 0.  0 0.  OGILMORE- JANAF                 NO
    .21580+05   .22627+05   .90197+01   .35340-04  -.11014+07   .60860+02 6000,0000 1
    .21580+05   .31251+05   .14268+02  -.28118-03  -.12173+09   .71196+0220000,0000 1 1,1132
 2. 7 0.  0 0.  0 0.  0 0.  0 0.  0 0.  OGILMORE - JANAF                N2
    .59500+00   .22449+05   .91676+01  -.31815-04  -.17126+07   .63781+02 6000,0000 1
    .59500+00   .22640+05   .37804+01   .69444-03   .35245+08   .63795+0220000,0000 1 1,0007
 1. 18 0.  0 0.  0 0.  0 0.  0 0.  0 0.  OCONVAIR ZPH-122 12/61         AR
    .00000      .14940+05   .41810+01   .12295-04   .37120+07   .48462+0210000,0000 1
    .00000      .14940+05   .41810+01   .12296-04   .37120+07   .48462+0220000,0000 1 1,2593

     ELEMENT   NITROGEN    OXYGEN       ANGON        ELECTRON
     BASE OF      N           O           AR            E-
 1. 7 2.  8 0.  0 0.  0 0.  0 0.  0 0.  OJANAF TAPE 7/71  9/64          NO2
    .79100+04   .34580+05   .12860+02   .38285-03  -.73138+06   .88819+02 2500,0000 1
    .79100+04   .34500+05   .13689+02   .32999-04  -.85391+06   .84802+0220000,0000 1 1,3303
 2. 7 1.  8 0.  0 0.  0 0.  0 0.  0 0.  OJANAF TAPE 7/71 12/64          N2O
    .19610+05   .30642+05   .13357+02   .54776+03  -.72634+06   .11624+02 2500,0000 1
    .19610+05   .36578+05   .14603+02   .44671-04  -.65269+06   .81601+0220000,0000 1 1,3130
 2. 7 3.  8 0.  0 0.  0 0.  0 0.  0 0.  OJANAF TAPE 7/71 12/64          N2O3
    .19800+05   .61892+05   .23037+02   .65259-03  -.12395+07   .12326+03 2500,0000 1
    .19800+05   .61812+05   .24463+02   .55216-04  -.83000+06   .12323+0320000,0000 1 1,6616
 2. 7 4.  8 0.  0 0.  0 0.  0 0.  0 0.  OJANAF TAPE 7/71  9/64          N2O4
    .21700+04   .78738+05   .29560+02   .81239-03  -.17088+07   .13496+03 2500,0000 1
    .21700+04   .78637+05   .31322+02   .70512-04  -.12048+07   .13492+0320000,0000 1 1,8042
 2. 7 5.  8 0.  0 0.  0 0.  0 0.  0 0.  OJANAF TAPE 7/71 12/64          N2O5
    .27000+04   .91618+05   .35291+02   .19109+03  -.10536+07   .15670+03 2500,0000 1
    .27000+04   .91590+05   .35681+02   .20051-04  -.11840+07   .15673+0320000,0000 1 1,9333
 3. 8 0.  0 0.  0 0.  0 0.  0 0.  0 0.  OJANAF TAPE 7/71  6/61          O3
    .34100+05   .30051+05   .13495+02   .27082-03  -.60869+06   .86101+02 2500,0000 1
    .34100+05   .30031+05   .13516+02   .14012-03  -.43034+06   .86094+0220000,0000 1 1,3630
 1. 7 3.  8 0.  0 0.  0 0.  0 0.  0 0.  OJANAF TAPE 7/71 12/64          NO3
    .17030+05   .49870+05   .19170+02   .26057-03  -.11252+07   .99914+02 2500,0000 1
    .17000+05   .49836+05   .19711+02   .24040-04  -.81434+06   .99902+0220000,0000 1 1,5220
 3. 7 0.  8 0.  0 0.  0 0.  0 0.  0 0.  OJANAF TAPE 7/71 12/70          N3
    .99000+05   .37294+05   .13563+02   .37648-03  -.79131+06   .81960+02 2500,0000 1
    .99000+05   .37247+05   .14657+02   .38305-04  -.37491+06   .81945+0220000,0000 1 1,2070
 1. 7 2.  8 1. 99 0.  0 0.  0 0.  0 0.  OJANAF TAPE 7/71 12/65          NO2-
   -.85850+05   .35358+05   .13250+02   .24018-03  -.88830+06   .84609+02 2500,0000 1
   -.85850+05   .35027+05   .13766+02   .21630-04  -.44102+06   .84590+0220000,0000 1 1,3303
 1. 7 1.  8-1. 99 0.  0 0.  0 0.  0 0.  OJANAF TAPE 7/71  6/66          NO+

    .23666+06   .22221+05   .75959+01   .50184+03  -.23354+06   .65350+02 2500,0000 1
    .23666+06   .22170+05   .86984+01   .71989-04  -.80765+06   .65340+0220000,0000 1 1,1132
 2. 7 1.  8-1. 99 0.  0 0.  0 0.  0 0.  OJANAF TAPE 7/71 12/70          N2O+
    .31069+06   .37537+05   .13975+02   .33753-03  -.65634+06   .86075+02 2500,0000 1
    .31069+06   .37494+05   .14570+02   .54482-04  -.35500+05   .86059+0220000,0000 1 1,3130
 1. 8 1. 99 0.  0 0.  0 0.  0 0.  0 0.  OJANAF TAPE 7/71  6/65          O-
    .24300+05   .13482+05   .49721+01  -.13736-05   .14490+05   .49295+02 2500,0000 1
    .24300+05   .13482+05   .45866+01  -.65339-07   .19415+05   .49295+0220000,0000 1  .8889
 2. 8 1. 99 0.  0 0.  0 0.  0 0.  0 0.  OJANAF TAPE 7/71 12/66          O2-
   -.11390+05   .21605+05   .87042+01   .16976-03  -.25141+06   .69312+02 2500,0000 1
   -.11390+05   .23508+05   .86744+01   .13303-03   .50901+06   .69106+0220000,0000 1 1,1444
 1. 7-1. 99 0.  0 0.  0 0.  0 0.  0 0.  OGILMORE AD654054 TO 50000K     N+
    .40746+06   .16975+05   .53702+01   .23593-04  -.40153+07   .49667+0210000,0000 1
    .40746+06  -.15432+06  -.15374+01   .20172-03   .65754+09   .12409+0220000,0000 1  .0016
 1. 7-2. 99 0.  0 0.  0 0.  0 0.  0 0.  OGILMORE AD654054 TO 50000K     N++
    .11300+07   .14439+05   .36637+01   .11590-03   .19550+08   .48652+0210000,0000 1
    .11300+07   .85143+05   .63744+01   .32866-04  -.31362+09   .64126+0220000,0000 1  .0016
 1. 8-1. 99 0.  0 0.  0 0.  0 0.  0 0.  OGILMORE AD654054 TO 50000K     O+
    .37351+06   .13866+05   .57119+01   .13310-03  -.14007+08   .48222+0210000,0000 1
    .37351+06  -.19830+06   .66613+00   .17433-03   .97521+09   .25310+0120000,0000 1  .8889
 1. 8-2. 99 0.  0 0.  0 0.  0 0.  0 0.  OGILMORE AD654054 TO 50000K     O++
    .11849+07   .15921+05   .53183+01   .17998-04  -.10612+08   .50221+0210000,0000 1
    .11849+07  -.34016+08   .48345+01   .42420-04   .86459+08   .45479+0220000,0000 1  .0009
 2. 8-1. 99 0.  0 0.  0 0.  0 0.  0 0.  OCONVAIR ZPH-122 12/61          O2+
    .27949+06   .24873+05   .59479+01   .42516-03   .18550+08   .67773+0210000,0000 1
    .27969+06   .24873+05   .59479+01   .42616-03   .19159+08   .67773+0220000,0000 1 1,1444
 2. 7-1. 99 0.  0 0.  0 0.  0 0.  0 0.  OCONVAIR ZPH-122 12061          N2+
    .35720+06   .25147+05   .13451+02  -.12794-03  -.22563+08   .65660+0210000,0000 .
    .35720+06   .25147+05   .13451+02  -.12794-03  -.22563+08   .65660+0220000,0000 1 1,0007
  UPDATE OF FAIL TEMPERATURES AND DIFFUSION FACTORS
        SPECIES    FAIL TEMPERATURE    DIFFUSION FACTOR
          N                                 .75550
          O                                 .70630
          O2                                .95530
          NO                                .99820
          N2                               1.02750
          N2O                              1.27200
```

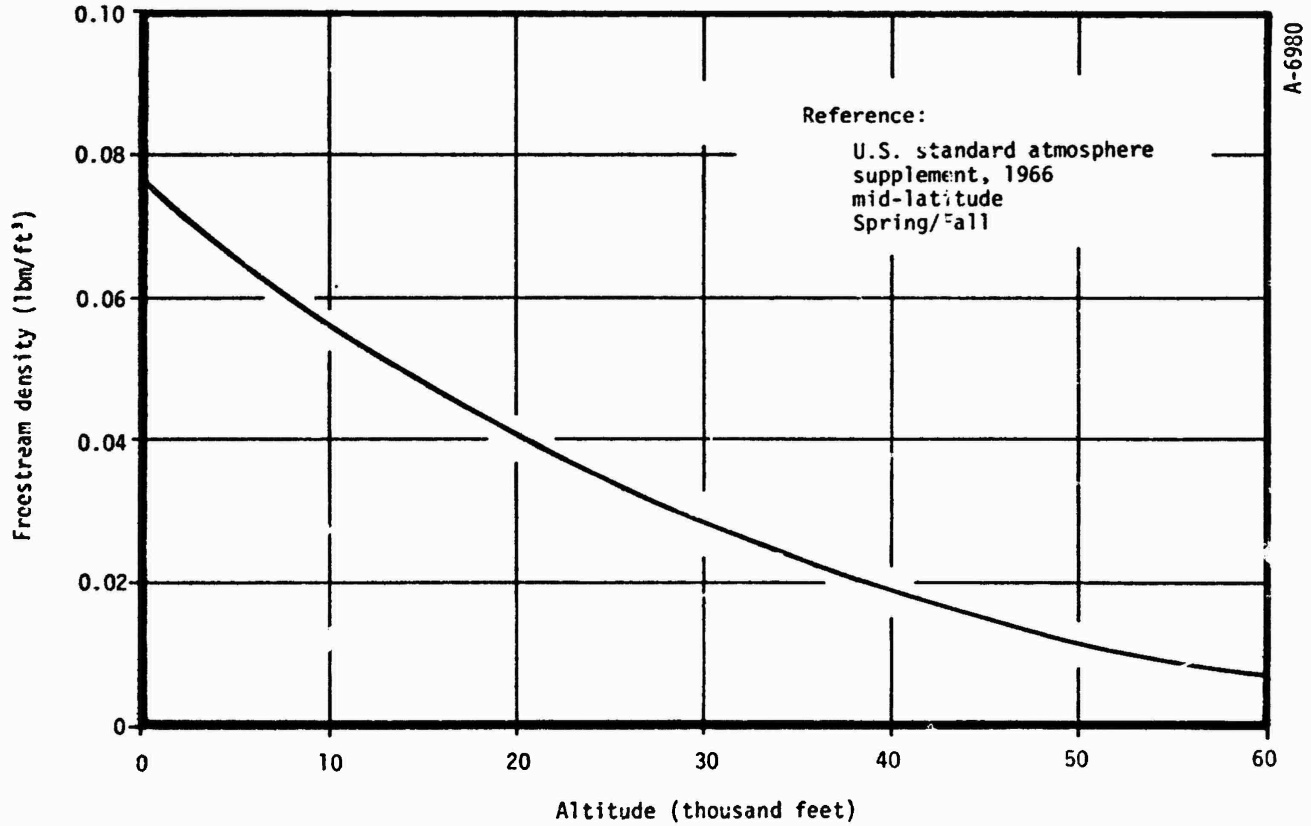

Figure A-1. Freestream density.

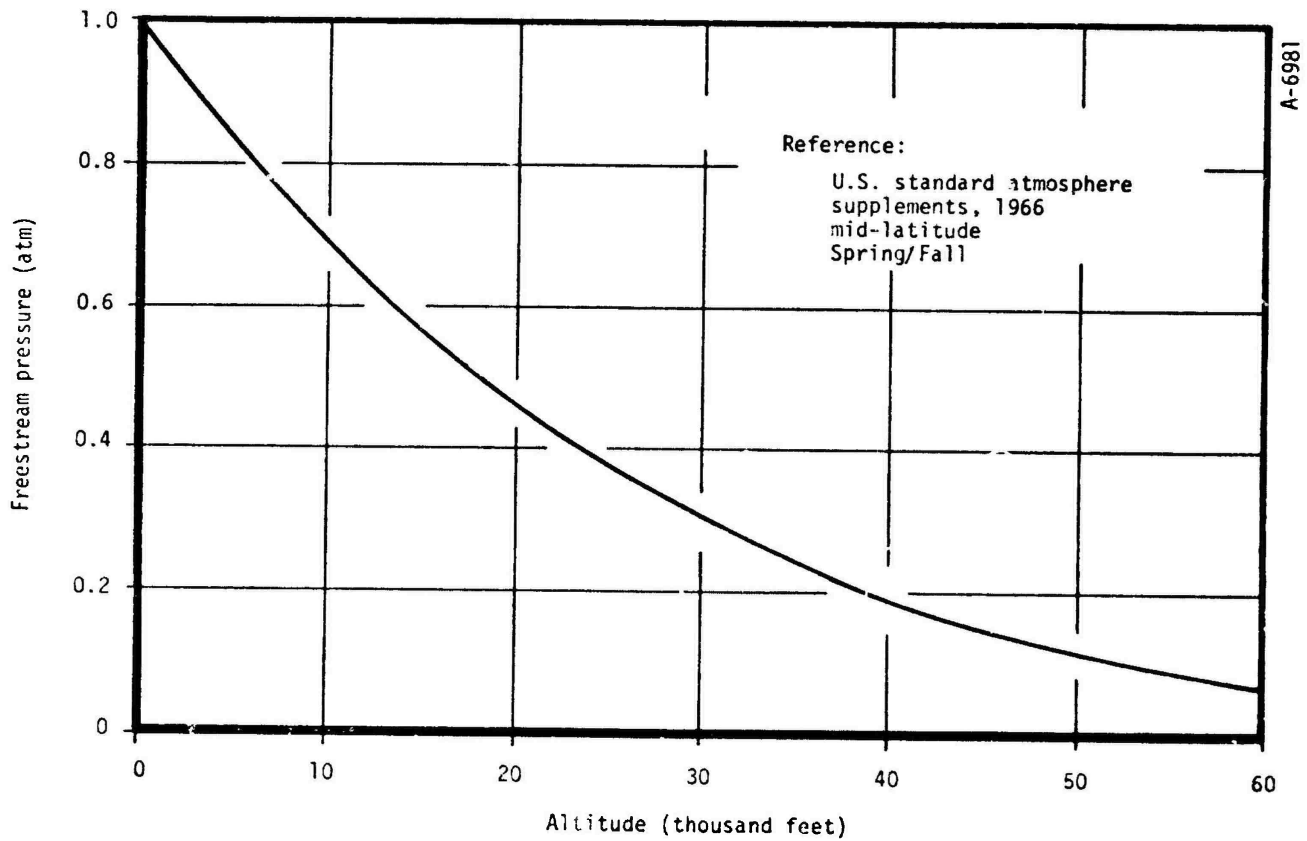

Figure A-2. Freestream pressure.

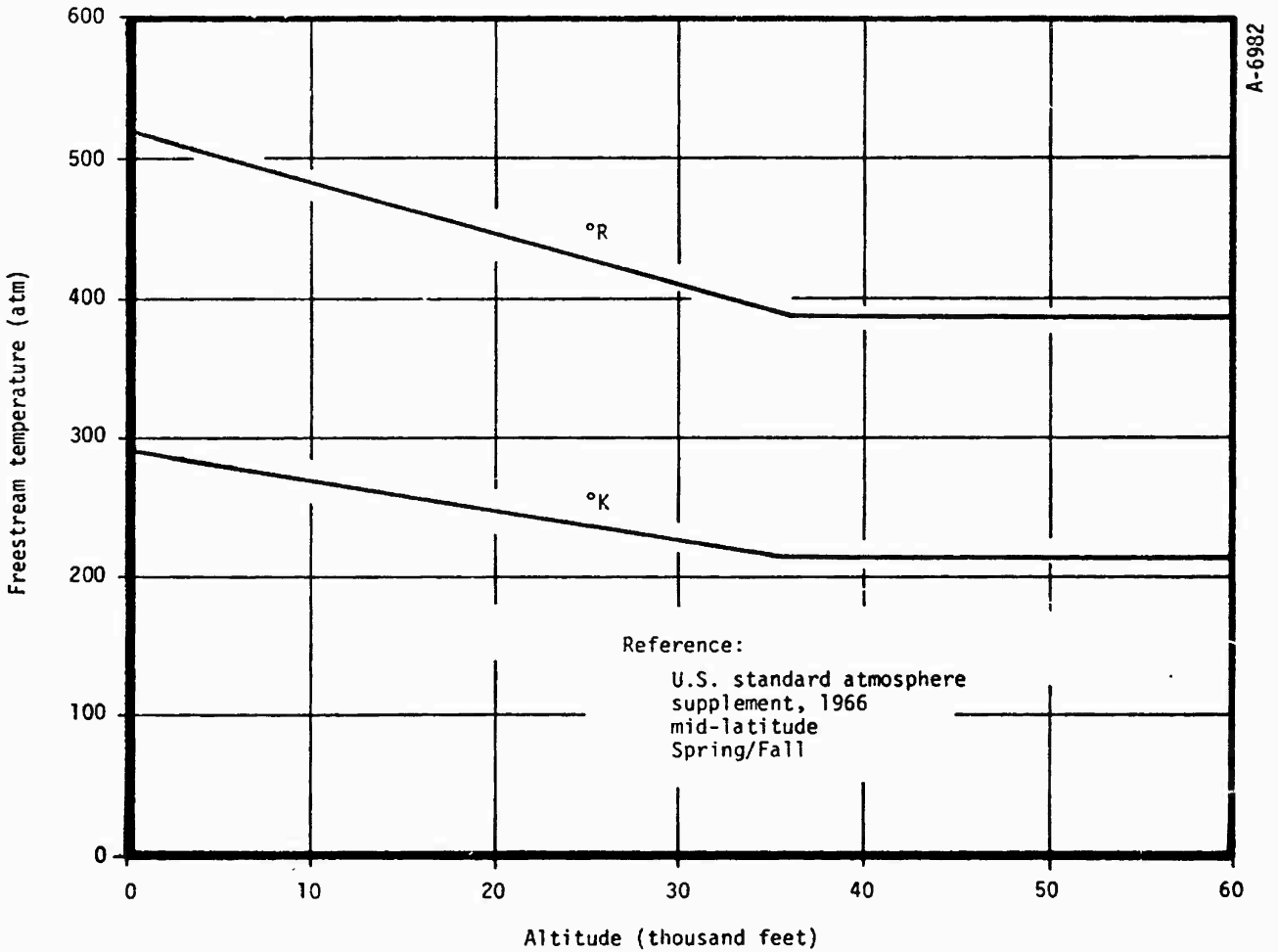

Figure A-3. Freestream temperature.

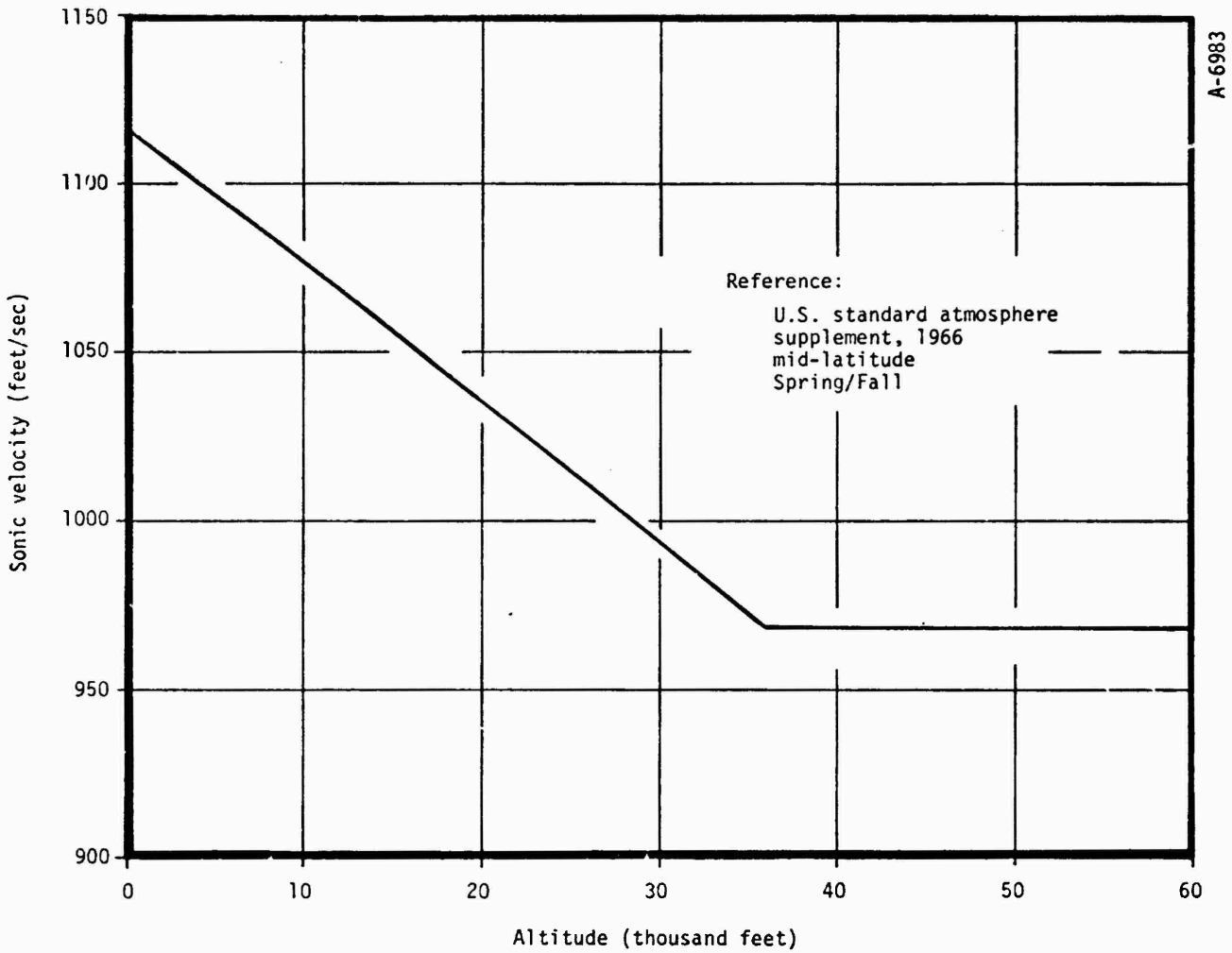

Figure A-4. Freestream sonic velocity.

TABLE A-2. SUMMARY OF TRAJECTORY PARAMETERS*

Parameters	Symbols	Units	Definition	Figure Number	Comments
Freestream Mach Number	M_∞	–	$\frac{U_\infty}{\sqrt{\sigma R T_\infty}}$	5	
Freesteam Unit Reynolds Number	Re_∞/ft	1/ft	$\frac{\rho_\infty U_\infty}{\mu_\infty}$	6	
Vehicle Stagnation Pressure	P_{t_2}	atm	–	7	Isentropic, real gas compression behind shock
Vehicle Total Enthalpy	H_t	Btu/lbm	$H_\infty + \frac{1}{2} U_\infty^2$	7	
Point Laminar Stagnation Momentum Thickness	$\frac{\theta_{stag}}{\sqrt{R_N}}$	$1/ft^{\frac{1}{2}}$	$\frac{0.332\mu}{\left[\rho\mu\sqrt{\frac{2P_{t_2}}{\rho}\left(1 - \frac{P_\infty}{P_{t_2}}\right)}\right]^{\frac{1}{2}}}$	8	Base on laminar flat plate Re_θ distribution
Sonic Point Unit Reynolds Number	Re^*/ft	1/ft	$\frac{\rho^* u^*}{\mu^*}$	9	ACE stagnation solution, isentropic real gas expansion to M = 1
Shock Density	$\rho_2/\rho_{water-0°c}$	–	$\rho_2/\rho_{water-0°c}$	10	
Shock Density Ratio	ρ_∞/ρ_2	–	ρ_∞/ρ_2	11	
Stagnation Point Shock Standoff Distance	Δ_s/R_N	–	–	12	Base on sphere cones. RAZZIB code
Particle Stagnation Pressure	P'_{t_2}	atm	–	13	Particle velocity equal to vehicle velocity, U_∞
Particle Total Enthalpy	H'_T	Btu/lbm	$H_2 + \frac{1}{2}[U_\infty - U_2]^2$	13	
Unit Weber Number	We/micron	1/micron	$\frac{\rho_2 U_\infty^2}{\sigma_{water - 0°C}}$	14	Particle We/micron = (We/micron)$(1 - \rho_\infty/\rho_2)^2$
Unit Reynolds Number	Re/micron	1/micron	$\frac{\rho_2 U_\infty}{\mu_2}$	15	Particle Re/micron = (Re/micron)$(1 - \rho_\infty/\rho_2)^2$
Particle Mach Number	M_s	–	$\frac{U_\infty - U_2}{C_2}$	16	

*The following nomeclature is used in this table:
- ∞ – freestream
- 2 – conditions behind shock
- * – sonic point property
- 2' – conditions behind particle shock
- t – total condition

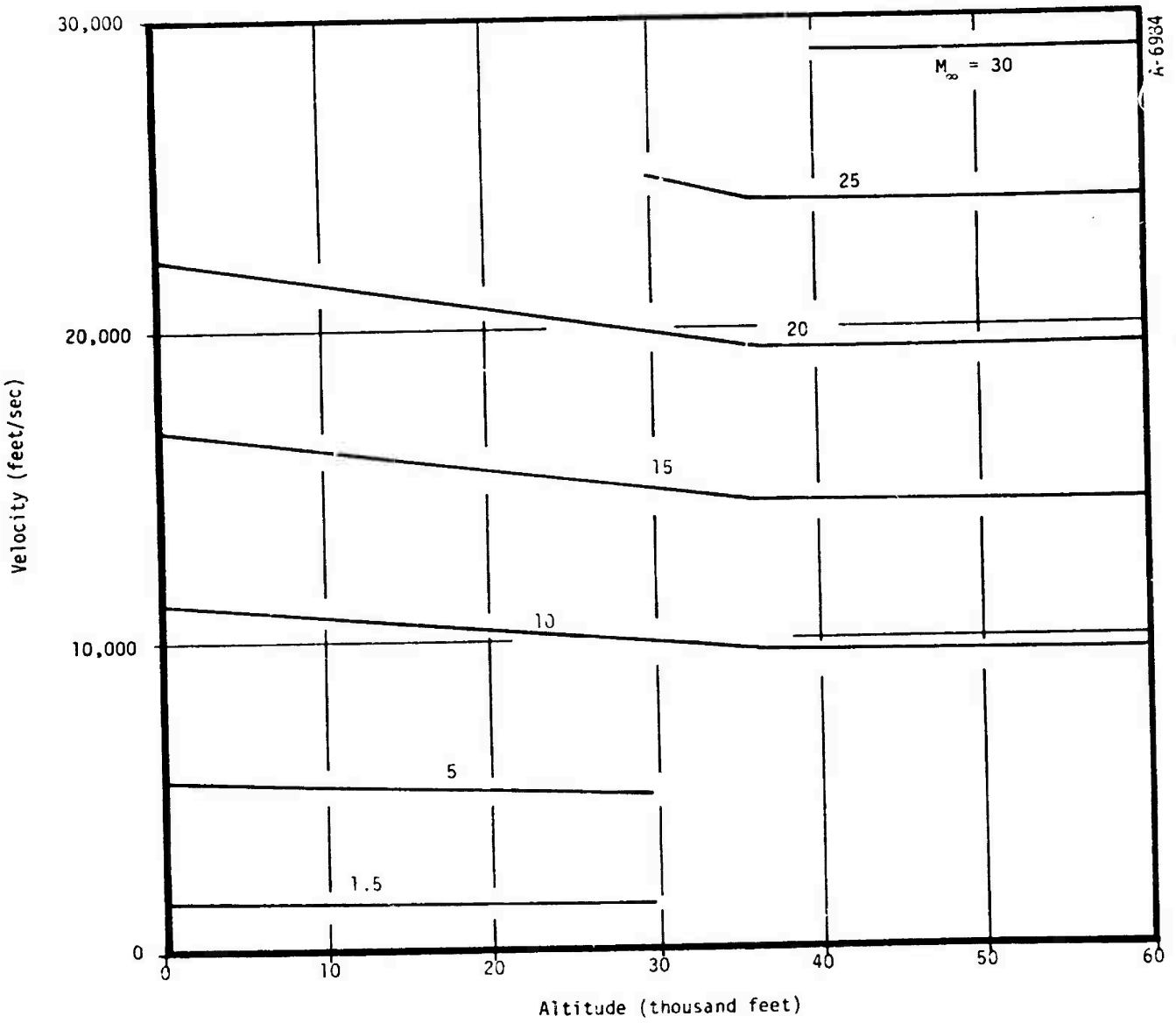

Figure A-5. Freestream Mach number (M_∞).

Figure A-6. Freestream unit Reynolds number (Re_∞/ft).

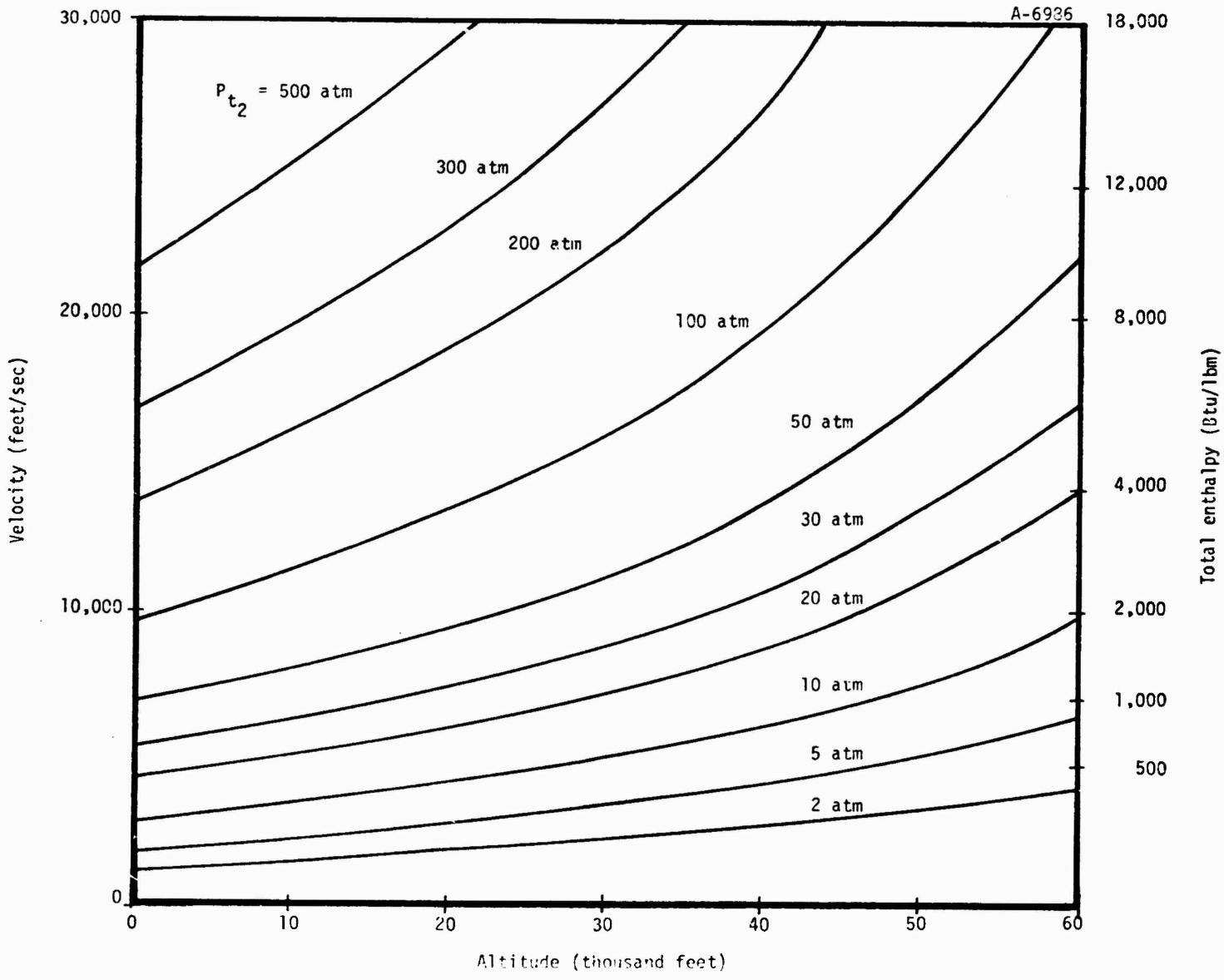

Figure A-7. Vehicle stagnation pressure and total enthalpy.

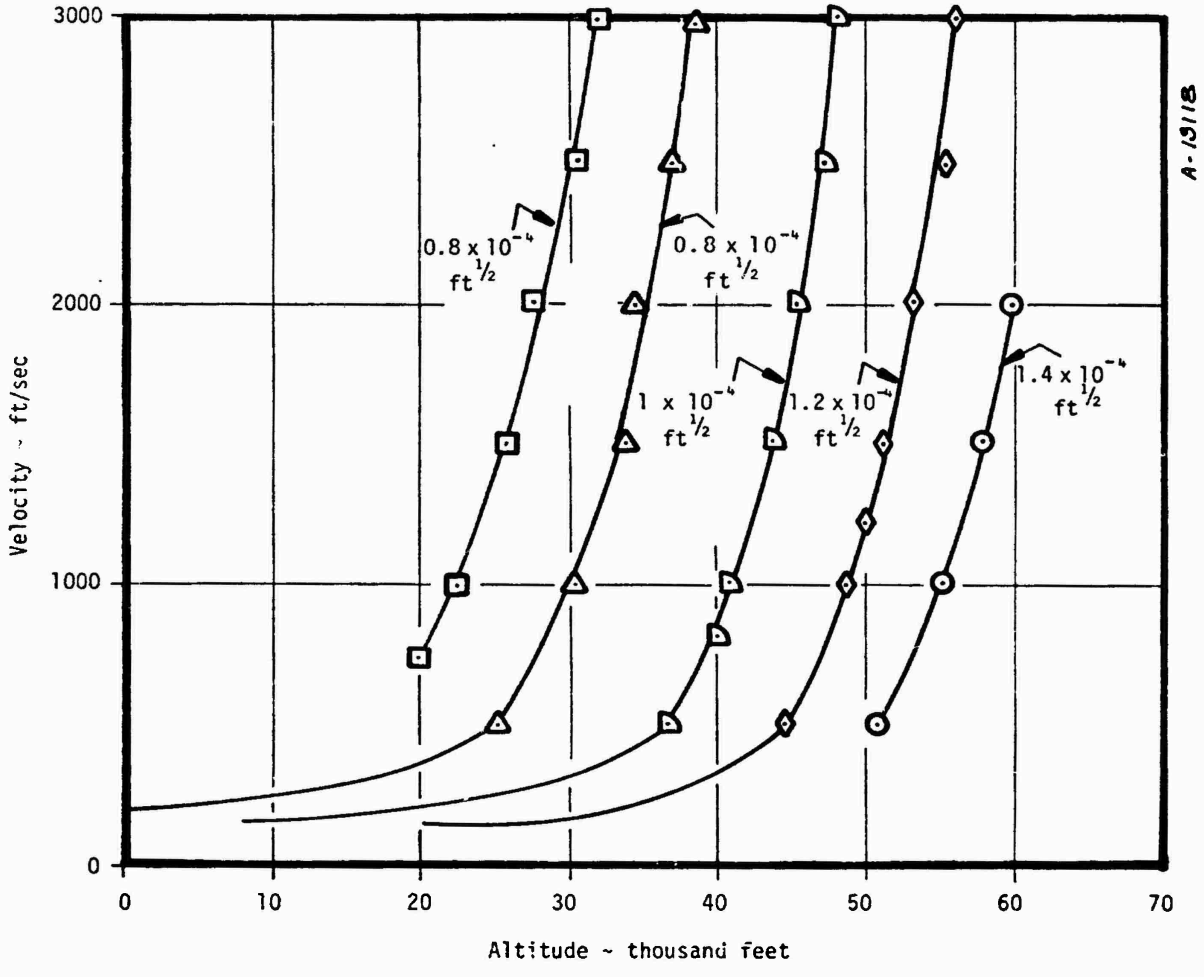

Figure A-8. Normalized stagnation point momentum thickness, $\theta^*_{stag}/\sqrt{R_N}$, [$ft^{1/2}$].

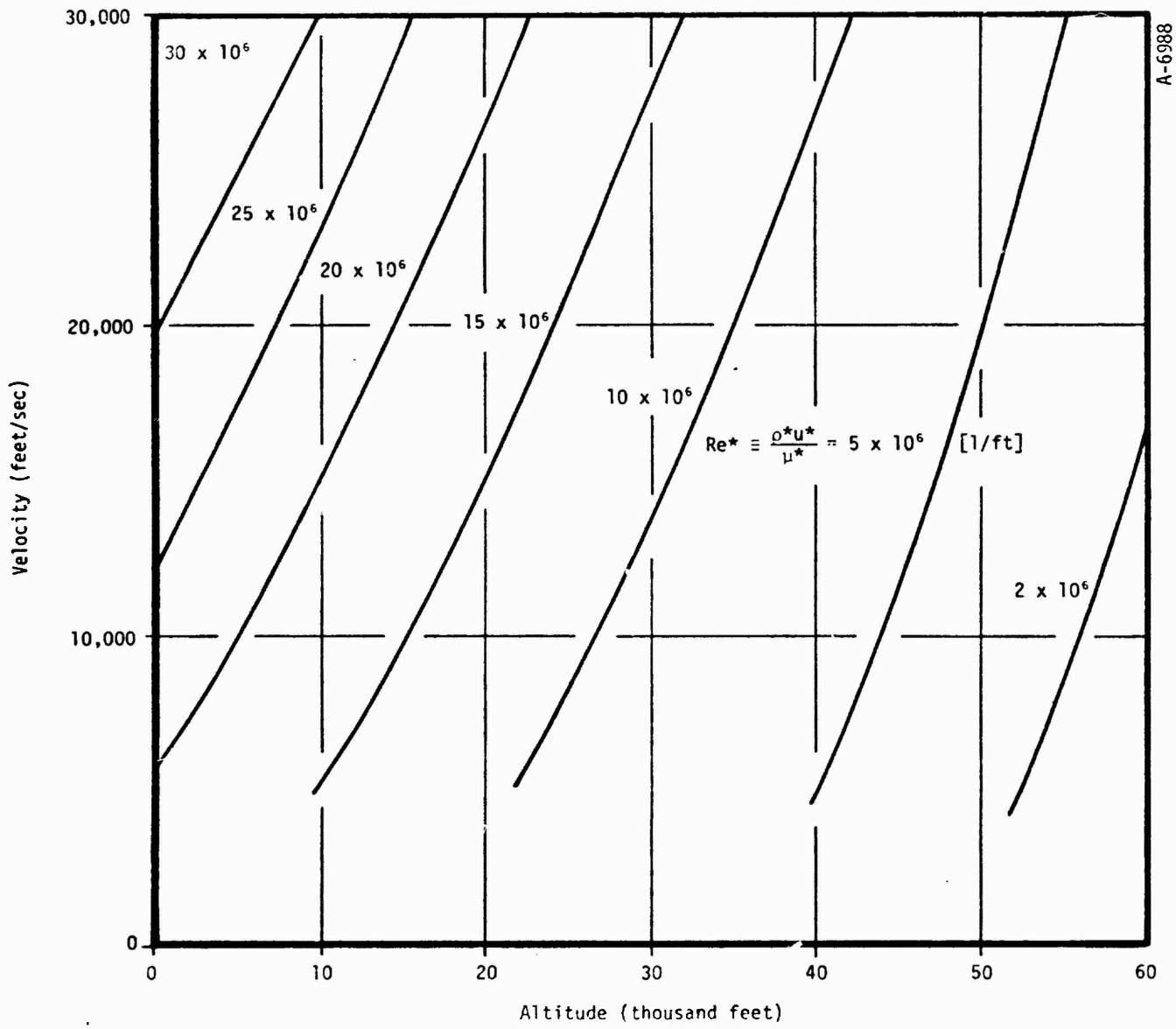

Figure A-9. Sonic point unit Reynolds number (Re*/ft).

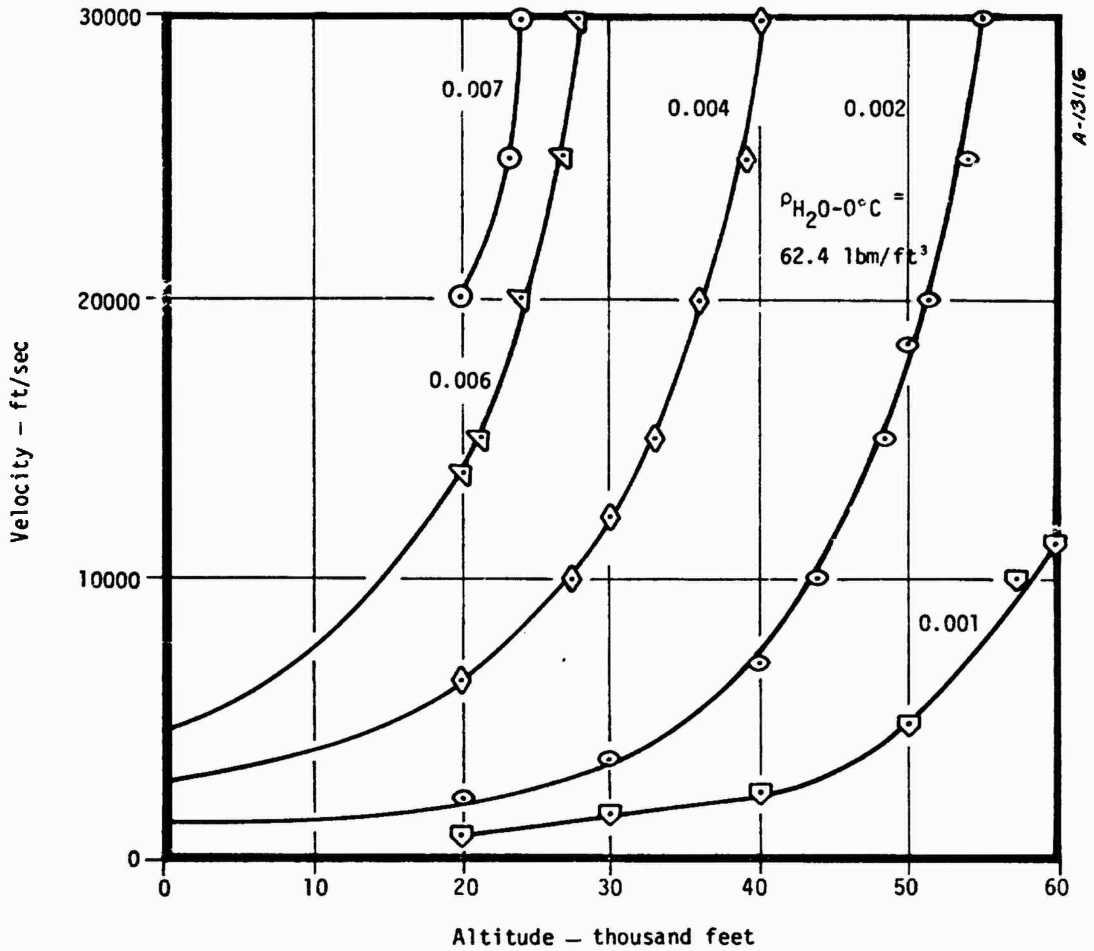

Figure A-10. Shock density ($\rho_2/\rho_{H_2O-0°C}$).

Figure A-11. Shock density ratio (ρ_∞/ρ_2).

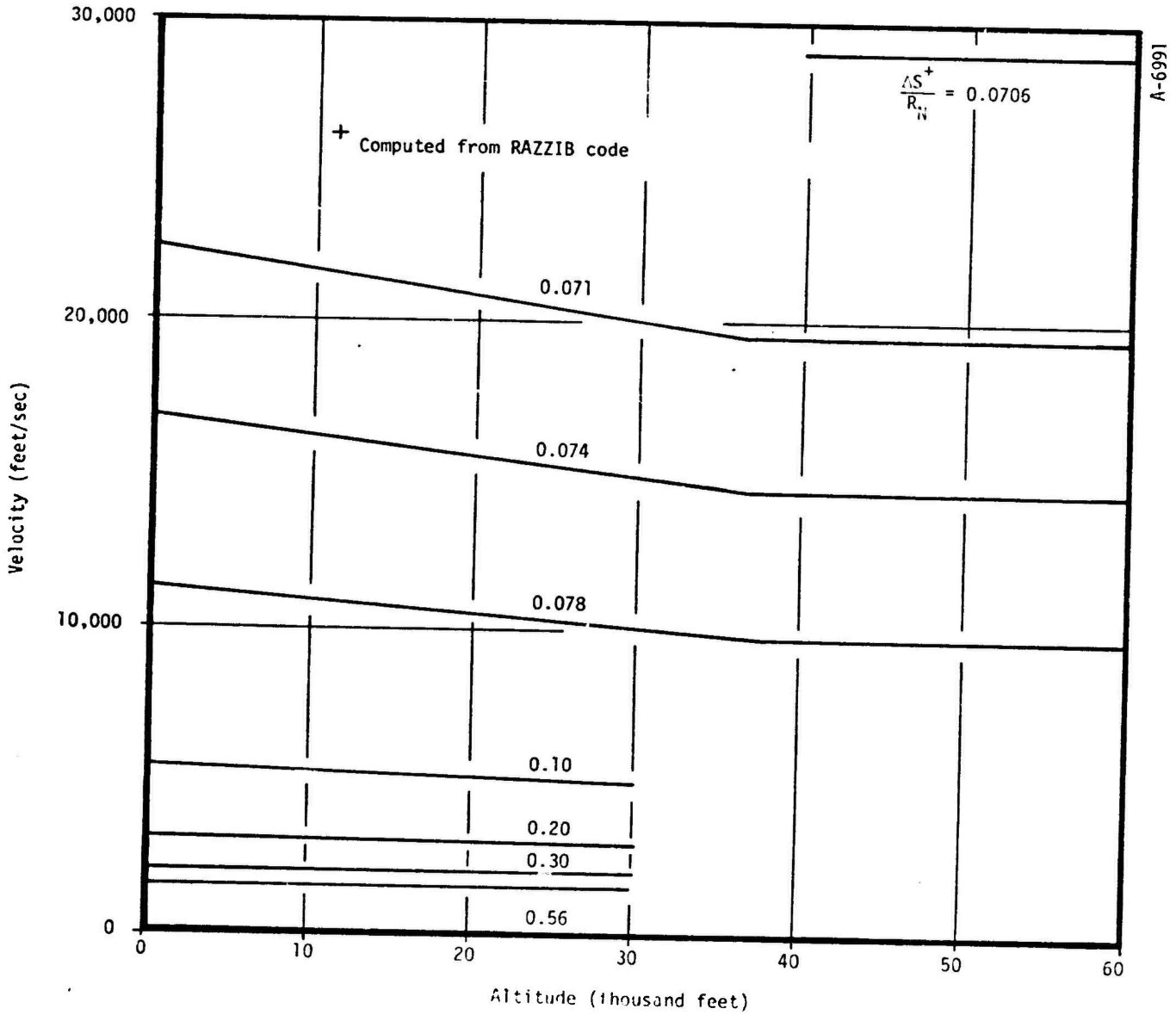

Figure A-12. Vehicle stagnation point shock standoff ($\Delta S/R_N$).

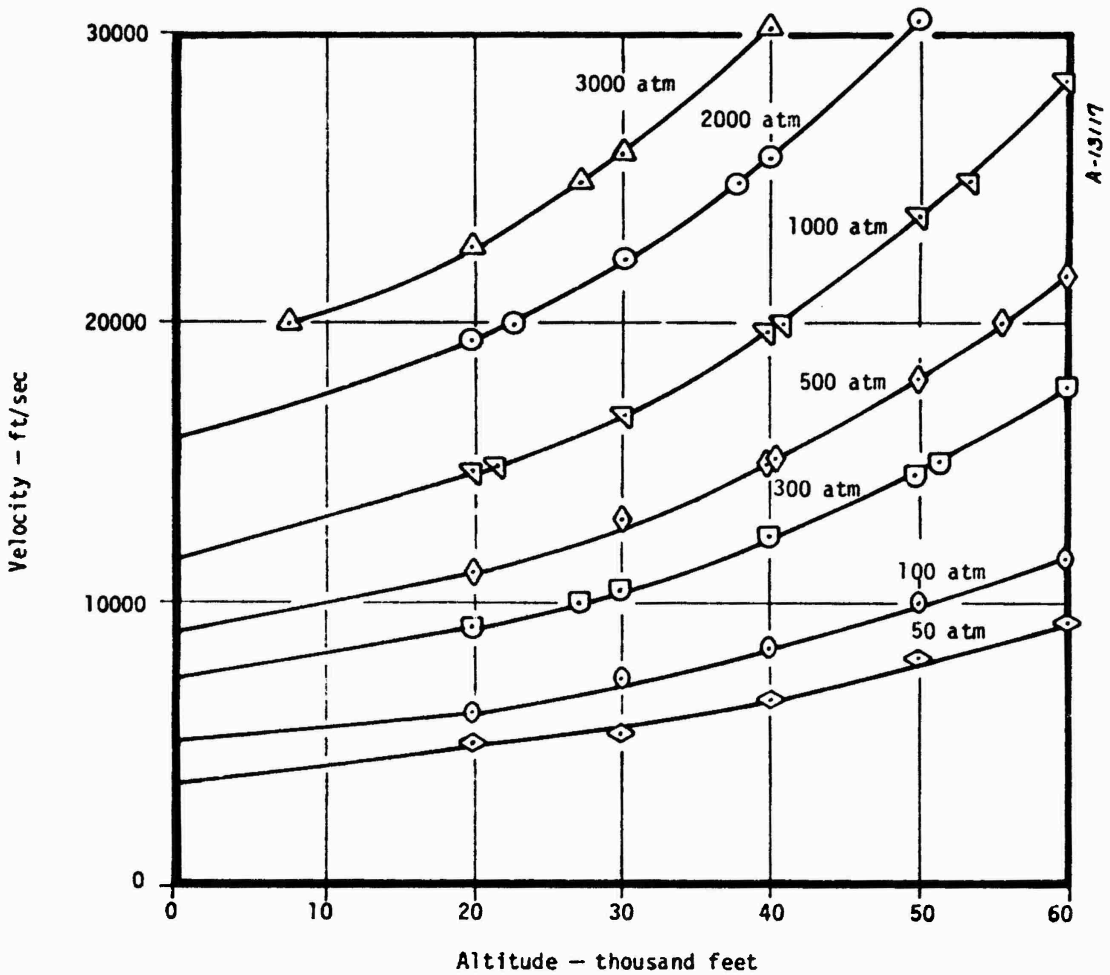

Figure A-13. Particle stagnation pressure.

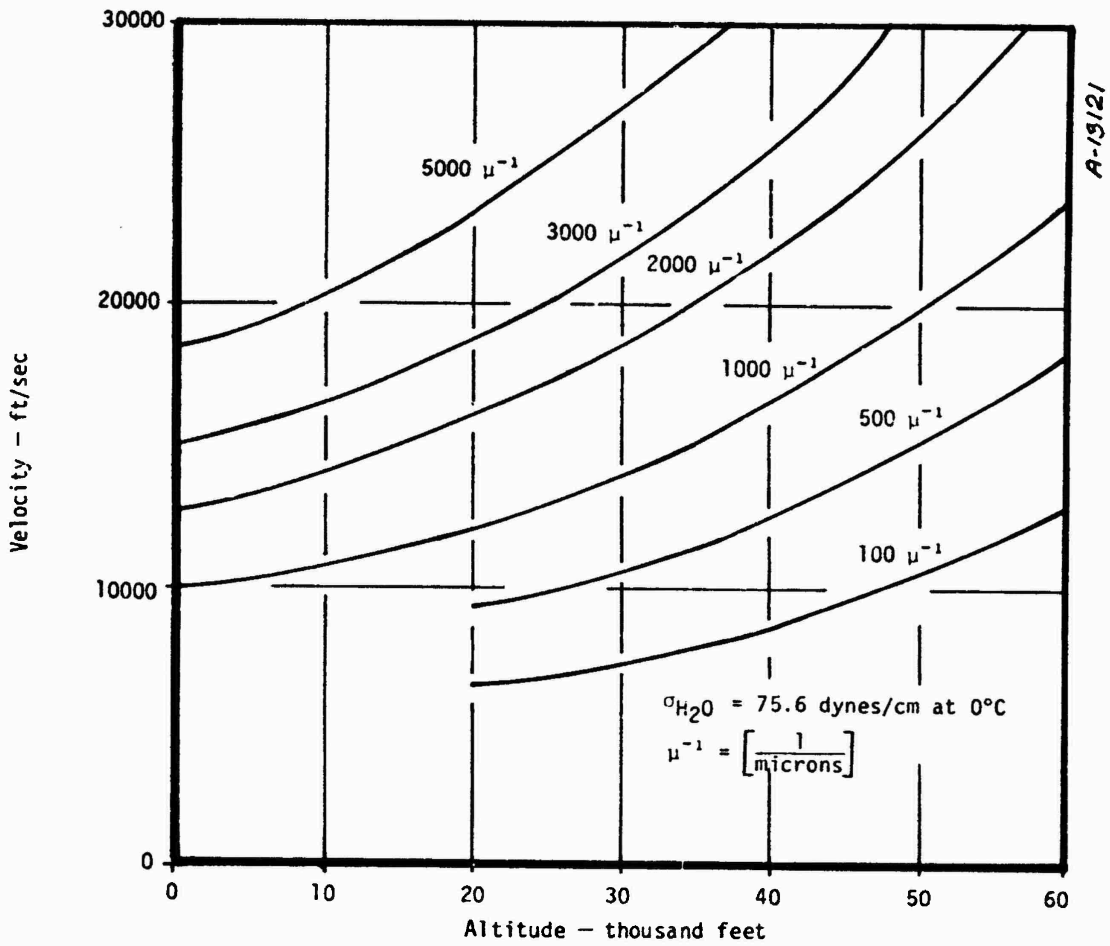

Figure A-14. Particle unit Weber number ($\rho_2 u_\infty^2/\rho_{H_2O}$).

Figure A-15. Particle unit Reynolds number ($Re = \rho_2 u_\infty / \mu_2$).

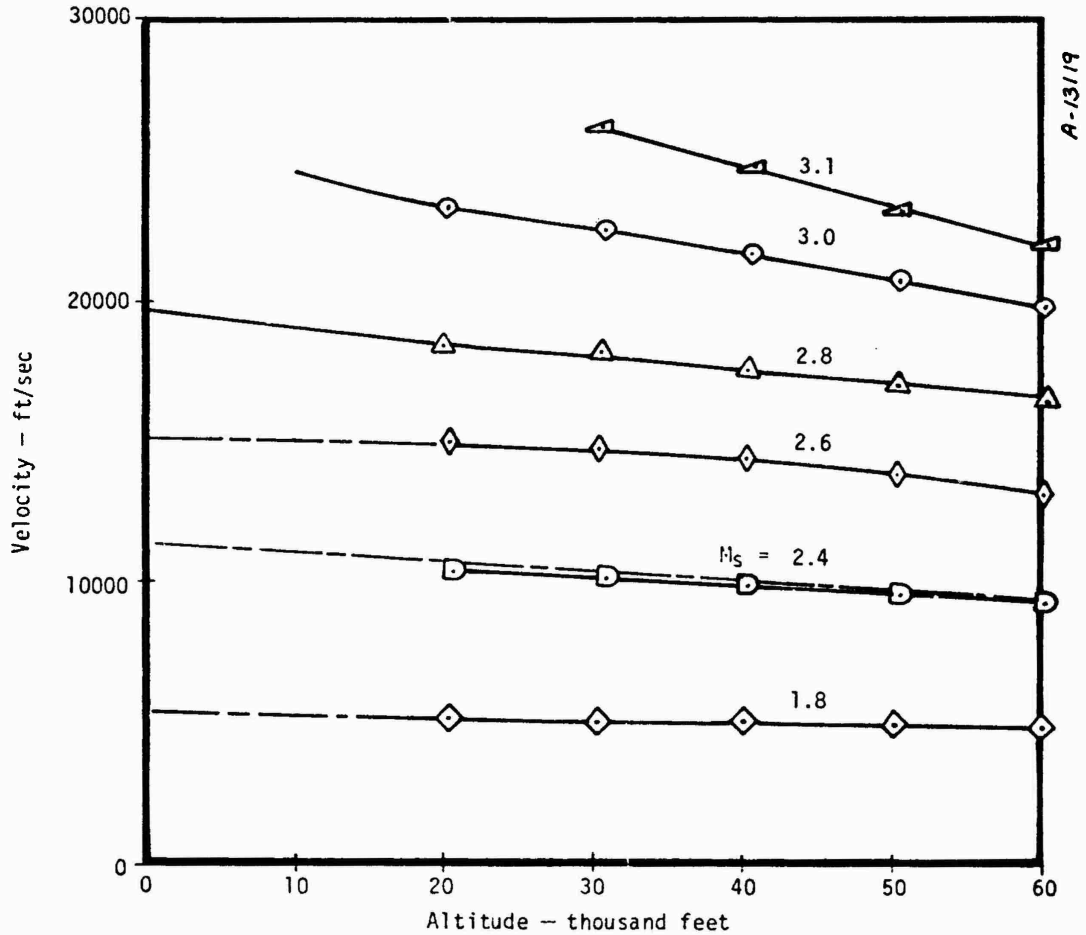

Figure A-16. Particle shock Mach number ($M_S = (u_{s_1} - u_2)/c_2$).

APPENDIX B

DETAILS OF LOCK'S FORMULATION

On the usual assumption that the change of velocity from U_2 to U_1 takes place in a layer of small thickness, and that v is everywhere small compared with u, the boundary layer equations are

$$u \frac{\partial u}{\partial x} + v \frac{\partial u}{\partial y} = \nu_1 \frac{\partial^2 u}{\partial y^2} \tag{B-1}$$

for the upper fluid, and

$$u \frac{\partial u}{\partial x} + v \frac{\partial u}{\partial y} = \nu_2 \frac{\partial^2 u}{\partial y^2} \tag{B-2}$$

for the lower fluid, where ν_1 and ν_2 are the kinematic viscosities of the two fluids.

The equation of continuity is

$$\frac{\partial u}{\partial x} + \frac{\partial v}{\partial y} = 0, \tag{B-3}$$

so that there exists a stream function ψ such that

$$u = \frac{\partial \psi}{\partial y} , \quad v = - \frac{\partial \psi}{\partial x} .$$

In order to solve Equation (A-1) we use the nondimensional variable

$$\eta_1 = \left(\frac{U_1}{\nu_1 x} \right)^{1/2} y \tag{B-4}$$

and look for a solution in which

$$\psi = (\nu_1 U_1 x)^{1/2} f_1(\eta_1). \tag{B-5}$$

Then

$$u = U_1 f_1'(\eta_1) \ , \tag{B-6}$$

$$v = \frac{1}{2}\left(\frac{U_1 \nu_1}{x}\right)^{1/2} \{\eta_1 f_1'(\eta_1) - f_1(\eta_1)\} \tag{B-7}$$

and

$$\frac{\partial u}{\partial y} = U_1 \left(\frac{U_1}{\nu_1 x}\right)^{1/2} f_1''(\eta_1) \ . \tag{B-8}$$

Equation (B-1) then reduces to

$$2\frac{d^3 f_1}{d\eta_1^3} + f_1 \frac{d^2 f_1}{d\eta_1^2} = 0 \ . \tag{B-9}$$

In the lower fluid it is convenient to use a different variable η_2 defined by

$$\eta_2 = \left(\frac{U_1}{\nu_2 x}\right)^{1/2} y \ , \tag{B-10}$$

so that

$$\eta_2 = \left(\frac{\nu_1}{\nu_2}\right)^{1/2} \eta_1 \ ,$$

and to put

$$\psi = (\nu_2 U_1 x)^{1/2} f_2(\eta_2) \ . \tag{B-11}$$

Then

$$u = U_1 f_2'(\eta_2) \ , \tag{B-12}$$

$$v = \frac{1}{2}\left(\frac{U_1 \nu_2}{x}\right)^{1/2} \{\eta_2 f_2'(\eta_2) - f_2(\eta_2)\} \tag{B-13}$$

and

$$\frac{\partial u}{\partial y} = U_1 \left(\frac{U_1}{\nu_2 x}\right)^{1/2} f_2''(\eta_2) \ . \tag{B-14}$$

Equation (B-2) then reduces to

$$2\frac{d^3f_2}{d\eta_2^3} + f_2\frac{d^2f_2}{d\eta_2^2} = 0 \ . \qquad \text{(B-15)}$$

Boundary Conditions

The boundary conditions at infinity are

$$u \to U_1 \quad \text{as} \quad \eta_1 \to +\infty$$

and

$$u \to U_2 \quad \text{as} \quad \eta_2 \to -\infty \ ,$$

so that

$$f_1' \to 1 \quad \text{as} \quad \eta_1 \to +\infty \qquad \text{(B-16)}$$

and

$$f_2' \to \frac{U_2}{U_1} \quad \text{as} \quad \eta_2 \to -\infty \ . \qquad \text{(B-17)}$$

Since the motion is steady, the interface between the fluids is streamline $\psi = 0$ which passes through the origin, and is therefore given by

$$f_1 = f_2 = 0 \ .$$

If η_2^0 is the value of η_2 such that $f_2(\eta_2^0) = 0$, then we must have also

$$f_1(\eta_2^0) = 0 \ ,$$

where

$$\eta_2^0 = \left(\frac{\nu_2}{\nu_1}\right)^{1/2} \eta_2^0 \ .$$

The other boundary conditions to be satisfied at the interface are that the velocity and the normal and transverse components of stress should be continuous.

APPENDIX C

HYDROMETEOR ACCELERATION AND MASS LOSS IN A SHOCK LAYER CONSIDERING BLOWING AND REAL GAS EFFECTS ON HEAT AND MASS TRANSFER

Jaffe (References C-1 and C-2) coupled the mass, momentum, and energy relations for an ablating particle in the shock layer of a high speed vehicle. This development is here modified to include the effects of blowing and real gas effects on droplet heat and mass transfer. In addition, a more appropriate dependence of heat transfer coefficient on shock and particle conditions is employed.

Particle Momentum

Force on a particle in the shock layer of a high speed vehicle is given adequately by a drag coefficient formulation as follows:

$$F = -C_D A_c \rho_2 u^2/2$$

ard

$$F = M_p A = M_p \frac{du}{dt} = M_p u \frac{du}{dx} \qquad \text{(C-1)}$$

where

C_D = drag coefficient*

A_c = particle cross sectional area, ft^2

ρ_2 = shock gas density, lbm/ft^3

u = particle velocity, ft/sec

For a spherical particle

$$M_p = 4\pi R_p{}^3 \rho_p/3 \qquad \text{(C-2)}$$

$$A_c = 4\pi R_p{}^2$$

Therefore,

$$\frac{1}{u}\frac{du}{dx} = -\frac{3}{8} C_D \left(\frac{\rho_2}{\rho_p}\right)\left(\frac{1}{R_p}\right) \qquad \text{(C-3)}$$

*For a sphere at hypersonic conditions, $C_D = 1.0$ approximately.

Nondimensionalizing gives

$$\frac{d\bar{u}}{d\bar{x}} = -K_D \frac{\bar{u}}{\bar{R}} \qquad \text{(C-4)}$$

where

$\bar{u} = u/u_\infty$

$\bar{x} = x/\Delta s$

$\bar{R} = R_p/R_{p,i}$

$K_D = \frac{3}{8} C_D \left(\frac{\rho_2}{\rho_p}\right) \left(\frac{\Delta s}{R_{p,i}}\right)$

Hydrometeor Ablation

Ablation of a hydrometeor particle can be evaluated by considering mass and energy conservation in combination with boundary layer and droplet properties. Mass and energy control volumes are illustrated in the following sketch.

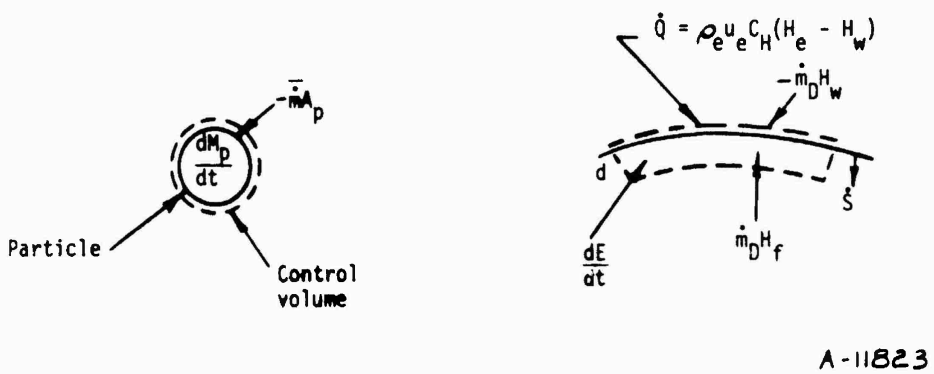

Mass Energy

Mass conservation gives

$$\frac{dM_p}{dt} = -\bar{\dot{m}}A_p \qquad \text{(C-5)}$$

where

$\bar{\dot{m}}$ = average surface mass loss flux

A_p = particle surface area = $4\pi R_p^2$

The average ablation flux, $\bar{\dot{m}}$, can be expressed in terms of the stagnation point values under the following conditions

- The leeside hemisphere experiences low heating and does not lose mass.
- The average windside hemisphere heat transfer and ablation rate is 71 percent of the stagnation point values (see Section 2).

That is,

$$\bar{\dot{m}} = 0.71\ \dot{m}_{D,SP}/2 \tag{C-6}$$

The quantity $\dot{m}_{D,SP}$ is the stagnation point mass removal flux and can be evaluated from energy conservation at the particle stagnation point.

In order to evalaute $\dot{m}_{D,SP}$, the control volume is chosen to be a thin layer extending from slightly above the ablating surface to beneath the thermal penetration depth. This energy control volume moves with the receding surface at a rate equal to the surface recession rate. Energy conservation for this control volume gives the following

$$\dot{Q} = \dot{m}_D(H_w - H_f) + \frac{dE}{dt} = \rho_e u_e C_H(H_e - H_w) \tag{C-7}$$

where

dE/dt = the rate of energy storage = 0 in steady state

$\rho_e u_e C_H$ = real gas film coefficient including blowing effects

H_e, H_w, H_f are enthalpies at the boundary layer edge, the surface of the droplet, and the initial temperature of the droplet, respectively

Equation (C-7) is useful when ablation and heat conduction reach steady state conditions and when the thermal penetration depth is much less than the droplet radius. A crude estimate of thermal penetration before vaporization begins is given by

$$-d = -K_w(T_{VAP} - T_i)/q_o \tag{C-8}$$

For R_p = 20 μm, M_∞ = 20, z = 15 kft

$$d = (0.88 \times 1.0^{-4}\ \text{Btu/ft-sec°R})(1165 - 400)/(10 \times 10^6\ \text{Btu/ft}^2\text{sec})$$

$$d = 0.67 \times 10^{-8}\ \text{ft} = 2 \times 10^{-3}\ \mu\text{m}$$

Thus, only a very thin surface layer of the 20 μm hydrometeor is affected by the heating prior to vaporization. Similar arguments show that thermal penetration and storage rate are negligible when vaporization occurs. Equation (C-7), therefo reduces to

$$\frac{\dot{m}_D}{\rho_e u_e C_H} = \frac{(H_e - H_w)}{(H_w - H_f)} \tag{C-9}$$

Equation (C-9) can be combined with the blowing effects correlation described in Section 2 to give $\dot{m}_D$ in terms of enthalpies, the non-blown transfer coefficient and the blowing parameter, λ.

That is, from Dorrance (Reference C-4),

$$\frac{C_H}{C_{H_o}} = \frac{2\lambda\dot{m}_D/\rho_e u_e C_{H_o}}{\exp(2\lambda\dot{m}_D/\rho_e u_e C_{H_o}) - 1} \tag{C-10}$$

where subscript "o" denotes non-blown values. Equation (C-10) can be rearranged to give

$$\dot{m}_D = \frac{\rho_e u_e C_{H_o}}{2\lambda} \ln(1 + 2\lambda\dot{m}_D/\rho_e u_e C_H) \tag{C-11}$$

Combining Equation (C-9) with Equation (C-11) and applying the result at the droplet stagnation point yields the desired result

$$\dot{m}_{D,SP} = \frac{\rho_e u_e C_{H_o,SP}}{2\lambda} \ln\left[1 + 2\lambda(H_e - H_w)/(H_w - H_f)\right] \tag{C-12}$$

At the hypersonic conditions of interest, the proper boundary layer edge enthalpy (H_e) for use with a stagnation point film coefficient is the total enthalpy behind the second shock, H'_{tot}; this enthalpy is generally large compared to the wall enthalpy, H_w. Also, the enthalpy difference, $H_w - H_f$, is the energy absorbed in heating and vaporizing a unit mass of the hydrometeor. The quantity has been termed the "heat of ablation", Q_p, and would include a heat of fusion if the hydrometeor were initially an ice particle. Approximations for the enthalpy terms can be used because the mass flux varies as the logarithm. For convenience, Equation (C-12) is expressed as

$$\dot{m}_{D,SP} = \frac{\rho_e u_e C_{H_o}}{2\lambda} \ln\left[1 + 2\lambda H'_{tot}/Q_P\right] \tag{C-13}$$

Combining Equations (C-5), (C-6), and (C-13) and substituting the mass of the particle gives

$$\frac{dM_p}{dt} = \frac{d}{dt}\left(4\pi R_p^3 \rho_D\right) = 4\pi R_p^2 \rho_p \frac{dR_p}{dt}$$

$$= -(4\pi R_p^2)\,\frac{0.71\rho_e u_e C_{H_o}\big]_{SP}\,\ell n\left[1 + 2\lambda H'_{tot}/Q_p\right]}{4\lambda} \qquad \text{(C-14)}$$

or

$$\frac{dR_p}{dt} = -\,\frac{0.71\rho_e u_e C_{H_o}\big]_{SP}\,\ell n\left[1 + 2\lambda H'_{tot}/Q_p\right]}{4\lambda\rho_p} \qquad \text{(C-15)}$$

To this point the development of the coupled mass, momentum, and energy equations describing the response of the hydrometeor is, except for the addition of blowing effects, quite parallel to that of Jaffe (References C-1 and C-2). Contrary to Jaffe, it is felt that for particles in supersonic flow, the heat transfer coefficient should be scaled as the particle velocity divided by the square root of the particle radius. This has justification in the theory of Fay and Riddell (Reference C-3) and in the numerical work performed by Bartlett and Putz (Reference C-4). Thus,

$$\rho_e u_e C_{H_o}\big]_{SP} = \rho_e u_e C_{H_o}\big]_{SP,i}\left(\frac{u}{u_\infty}\right)\left(\frac{R_{p,i}}{R_p}\right)^{0.5} \qquad \text{(C-16)}$$

Jaffe (References C-1 and C-2) utilized a Nusselt number, based on initial conditions, which varied inversely with particle radius and independent of velocity. BLIMP calculations and the correlation given in Section 2 provide the initial condition heat transfer coefficient, $\rho_e u_e C_{H_o\,SP,i}$. Equation (C-16) can, therefore, be written:

$$\frac{dR_p}{dt} = -\,\frac{0.71\rho_e u_e C_{H_o}\big]_{SP,i}\,\ell n(1 + 2\lambda H'_{tot}/Q_p)}{4\lambda\rho_p}\,\frac{u}{u_\infty}\left(\frac{R_{p_i}}{R_p}\right)^{1/2} \qquad \text{(C-17)}$$

Normalizing Equation (C-17) and converting to path length as the independent variable gives

$$\bar{R}^{1/2}\,\frac{d\bar{R}}{d\bar{x}} = -K'_E \qquad \text{(C-18)}$$

where

$$\bar{R} = R_p/R_{p_i}$$

$$\bar{x} = x/\Delta s$$

$$K'_E = \frac{0.71\rho_e u_e C_{H_o}\big]_{SP,i}\,\ell n(1 + 2\lambda H'_{tot}/Q_p)\Delta s}{4\lambda\rho_p u_\infty R_p}$$

$$dt = \frac{dx}{u} = \frac{\Delta s\, d\bar{x}}{u}$$

Boundary condition on Equation (C-17) is $\bar{R} = 1$ at $\bar{x} = 0$. Integration gives

$$\bar{R} = \left(1 - \frac{3}{2} K_E' \bar{x}\right)^{2/3} \tag{C-19}$$

For the spherical particle

$$\frac{M_P}{M_{P,i}} = \frac{\frac{4}{3}\pi R_P^3 \rho_P}{\frac{4}{3}\pi R_{P,i}^3 \rho_P} = \bar{R}^3 = \left(1 - \frac{3}{2} K_E' \bar{x}\right)^2 \tag{C-20}$$

At the nosetip surface where $\bar{x} = 1.0$

$$\frac{M_P}{M_{P,i}} = \left(1 - \frac{3}{2} K_E'\right)^2 \tag{C-21}$$

In Equation (C-21) K_E' must be less than 2/3 for the particle survival to the nosetip surface. K_E' greater than 2/3 corresponds to complete particle ablation in the shock layer. Equation (C-18) shows that the particle radius reduction is not a significant function of the particle slowdown since the drag constant, K_D, does not enter the relation. Some elements of the energy constant, K_E', such as H_{tot}', are dependent on the gas/particle relative velocities. Thus, for conditions of significant slowdown, Equation (C-21), for example, would become inaccurate. The equations are accurate for conditions of interest, however.

Coupled Ablation and Slowdown

Combining Equation (C-19) with (C-4) using the boundary condition $\bar{u} = 1$ at $\bar{x} = 0$ yields

$$\bar{u} = \exp\left\{-\frac{2K_D}{K_E'}\left[1 - \left(1 - \frac{3}{2} K_E' \bar{x}\right)^{1/3}\right]\right\} \tag{C-22}$$

where $K_E' > 2/3$ for particle demise in shock layer. Parametric results using Equations (C-19) and (C-21) are shown in Figure C-1.

Hydrometeor mass and velocity attenuation by the technique presented above is somewhat less than the results obtained using the technique of Jaffe (Reference C-2), which gives

$$\bar{x} = \frac{1}{K_D}\left\{(\bar{R} - 1) + \left(1 + \frac{K_E}{K_D}\right) \ln\left[1 - \frac{K_D}{K_E}(\bar{R} - 1)\right]\right\}$$

$$\bar{u} = \left[\left(1 + \frac{K_D}{K_E}\right) - \frac{K_D \bar{R}}{K_E}\right]^{-1} \tag{C-23}$$

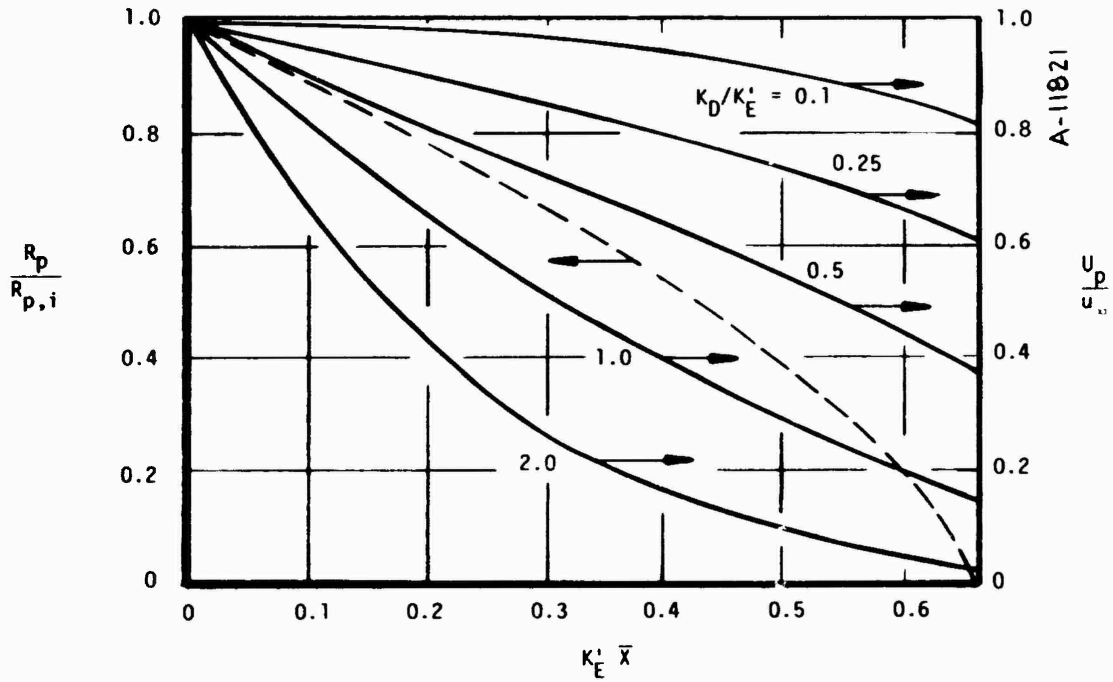

Figure C-1. Hydrometeor radius and velocity attenuation including blowing and real gas heat transfer.

where

$$K_D = \frac{3}{8} C_D \left(\frac{\rho_2}{\rho_p} \right) \frac{\Delta s}{R_{p,i}}$$

$$K_E = \frac{K_m Nu_m \Delta T_m \Delta s}{2 \rho_p Q_p U_\infty R_{p,i}^2}$$

Results are not drastically different because Nusselt number correlations give less heat transfer than predicted for real gas conditions by BLIMP whereas the BLIMP heat transfer results have been reduced for blowing effects.

REFERENCES FOR APPENDIX C

C-1. Jaffe, N. A., "Particle Deceleration and Heating in a Hypersonic Shock Layer," Aerotherm TN-73-18, February 1973.

C-2. Jaffe, N. A., "Droplet Dynamics in a Hypersonic Shock Layer," AIAA J., Vol. 11, No. 11, pp. 1562-1564, November 1973.

C-3. Fay, J. A. and Riddell, F. R., "Theory of Stagnation Point Heat Transfer in Dissociated Air," Jour. Aero. Sci., Vol. 25, 73-85, p. 121, 1958.

C-4. Bartlett, E. P. and Putz, K. E., "Heat Transfer and Ablation-Rate Correlations for Re-Entry Heat Shield and Nosetip Applications," Journal of Spacecraft and Rockets, 1973, p. 15.